Geoscience Frontiers xxx (xxxx) 101522

Contents lists available at ScienceDirect

Geoscience Frontiers

journal homepage: www.elsevier.com/locate/gsf

Research Paper

Deformation history and processes during accretion of seamounts in subduction zones: The example of the Durkan Complex (Makran, SE Iran)

Edoardo Barbero[a,b], Maria Di Rosa[c], Luca Pandolfi[c,d], Morteza Delavari[e], Asghar Dolati[e], Federica Zaccarini[f], Emilio Saccani[a,*], Michele Marroni[c,d]

[a] Dipartimento di Fisica e Scienze della Terra, Università di Ferrara, 44123 Ferrara, Italy
[b] Istituto di Geoscienze e Georisorse, Consiglio Nazionale delle Ricerche (CNR), 10125 Torino, Italy
[c] Dipartimento di Scienze della Terra, Università di Pisa, 56126 Pisa, Italy
[d] Istituto di Geoscienze e Georisorse, Consiglio Nazionale delle Ricerche (CNR), 56124 Pisa, Italy
[e] Faculty of Earth Sciences, Kharazmi University, Tehran 15719-19911, Iran
[f] Department of Applied Geological Sciences and Geophysics, University of Leoben, 8700 Leoben, Austria

ARTICLE INFO

Article history:
Received 15 July 2022
Received in revised form 17 November 2022
Accepted 1 December 2022

Handling Editor: I. Safonova

Keywords:
Underplated seamount
Makran Accretionary Prism
Tectono-sedimentary evolution
Tectono-metamorphic evolution
Cretaceous
Iran

ABSTRACT

The Durkan Complex is a tectonic element of the Makran Accretionary Prism (SE Iran) that includes fragments of Late Cretaceous seamounts. In this paper, the results of map- to micro-scale structural studies of the western Durkan Complex are presented with the aim to describe its structural and tectono-metamorphic evolution. The Durkan Complex consists of several tectonic units bordered by mainly NNW-striking thrusts. Three main deformation phases (D_1, D_2, and D_3) are distinguished and likely occurred from the Late Cretaceous to the Miocene-Pliocene. D_1 is characterized by sub-isoclinal to close and W-verging folds associated with an axial plane foliation and shear zone along the fold limbs. This phase records the accretion of fragments of the seamount within the Makran at blueschist facies metamorphic conditions (160–300 °C and 0.6 – 1.2 GPa). D_2 is characterized by open to close folds with sub-horizontal axial plane that likely developed during the exhumation of previously accreted seamount fragments. An upper Paleocene – Eocene siliciclastic succession unconformably sealed the D_1 and D_2 structures and is, in turn, deformed by W-verging thrust faults typical of D_3. The latter likely testifies for a Miocene - Pliocene tectonic reworking of the accreted seamount fragments with the activation of out of sequence thrusts. Our results shed light on the mechanism of accretion of seamount materials in the accretionary prisms, suggesting that seamount slope successions favour the localization and propagation of the basal décollement. This study further confirms that the physiography of the subducting plates plays a significant role in the tectonic evolution of the subduction complexes.

© 20XX

1. Introduction

Seamounts are topographic highs of the seafloor ranging in height from 50~100 m to ~8 km (Hillier and Watts, 2007; Wessel et al., 2010). As elements of the oceanic plates, seamounts are passively carried toward convergent margins and their fate is the interaction with the frontal part of subduction zones. Seamounts-subduction zones interactions have been observed in several present-day convergent margins, such as the Nankai (Bangs et al., 2006), Hikurangi (Barnes et al., 2020), Japan (Lallemand et al., 1989), Costa Rica (von Huene et al., 2004), and Northern Chile (Geersen et al., 2015). Geophysical data from these subduction zones show that seamounts of different sizes are likely subducted (e.g., Lallemand et al., 1989; von Huene and Lallemand, 1990; Watts et al., 2010). Data from modern and fossil subduction complexes, as well as numerical modelling indicate that seamount fragments are transferred from the subducting plate to the accretionary prism with different mechanisms. These include either deformation within the subduction channel (e.g., Cloos and Shreve, 1988, 1996), or accretion via decapitation of seamount summit by the basal décollement of the prism (e.g., Cloos and Shreve, 1996; Bangs et al., 2006; Watts et al., 2010; Yang et al., 2015), or again offscraping and underplating of thrust-bounded assemblages at both shallow (4–8 km) and deep structural levels (20–30 km) of the prism (Isozaki et al., 1990; Isozaki, 1997; Park et al., 1999; Ueda, 2005; Vannucchi et al., 2006; Clarke et al., 2018; Bonnet et al., 2020; Zeng et al., 2021; Yang et al., 2022). In this complex scenario it is not completely clear which are those factors controlling deformation mechanisms and localization of the basal décollement

* Corresponding author.
E-mail address: sac@unife.it (E. Saccani).

https://doi.org/10.1016/j.gsf.2022.101522
1674-9871/© 20XX

UNCORRECTED PROOF

Note: Low-resolution images were used to create this PDF. The original images will be used in the final composition.

below, inside, or above the subducting seamount. Moreover, subduction of seamounts may influence the seismic activity at modern subduction zones either promoting or inhibiting large earthquakes ruptures and their propagation (e.g., Scholz and Small, 1997; Kodaira et al., 2000; Bilek et al., 2003; Watts et al., 2010 and reference therein; Wang and Bilek, 2011; Geersen et al., 2015; Sun et al., 2020).

Improving the knowledge on the role of subducted seamounts in subduction zones is, therefore, a key aspect for understanding the tectonic evolution of both fossil and active subduction zones. Complementary data with respect to geophysics and seismological dataset on modern convergent margins can be obtained from structural investigations of fossil seamounts accreted in ancient accretionary prisms or within collisional belts. To this purpose, the western Durkan Complex in the Makran Accretionary Prism (SE Iran Fig. 1a, b) represents an excellent case-study. In fact, according to some authors, this Complex includes tectono-sedimentary assemblages derived from the deformation of both continental and oceanic domains (McCall, 1985; Glennie et al., 1990; Hunziker et al., 2015; Burg, 2018). The oceanic assemblages are largely exposed in the western sector where they have recently been interpreted as representing a Late Cretaceous tectonically disrupted seamount chain (Barbero et al., 2021a, b), whereas the continental parts are documented in the eastern sector of the Durkan Complex (Hunziker et al., 2015). This complex has been deformed during the convergent stages associated to the northward subduction of the NeoTethys Ocean below the Eurasia margin (McCall and Kidd, 1982; Glennie et al., 1990; Hunziker, 2014; Burg, 2018; Moghadam et al., 2022). However, no detailed structural data are available in literature and, therefore, the deformation history of this complex remains poorly constrained. In this paper, we present the results of a new multiscale structural study to describe the structural setting and evolution of the Durkan Complex in the western North Makran (i.e., the oceanic part of the complex). This approach allows us to define the role of the Durkan Complex in the tectonic history of the Makran Accretionary Prism. Finally, we also discuss the implication of these data for a better under-

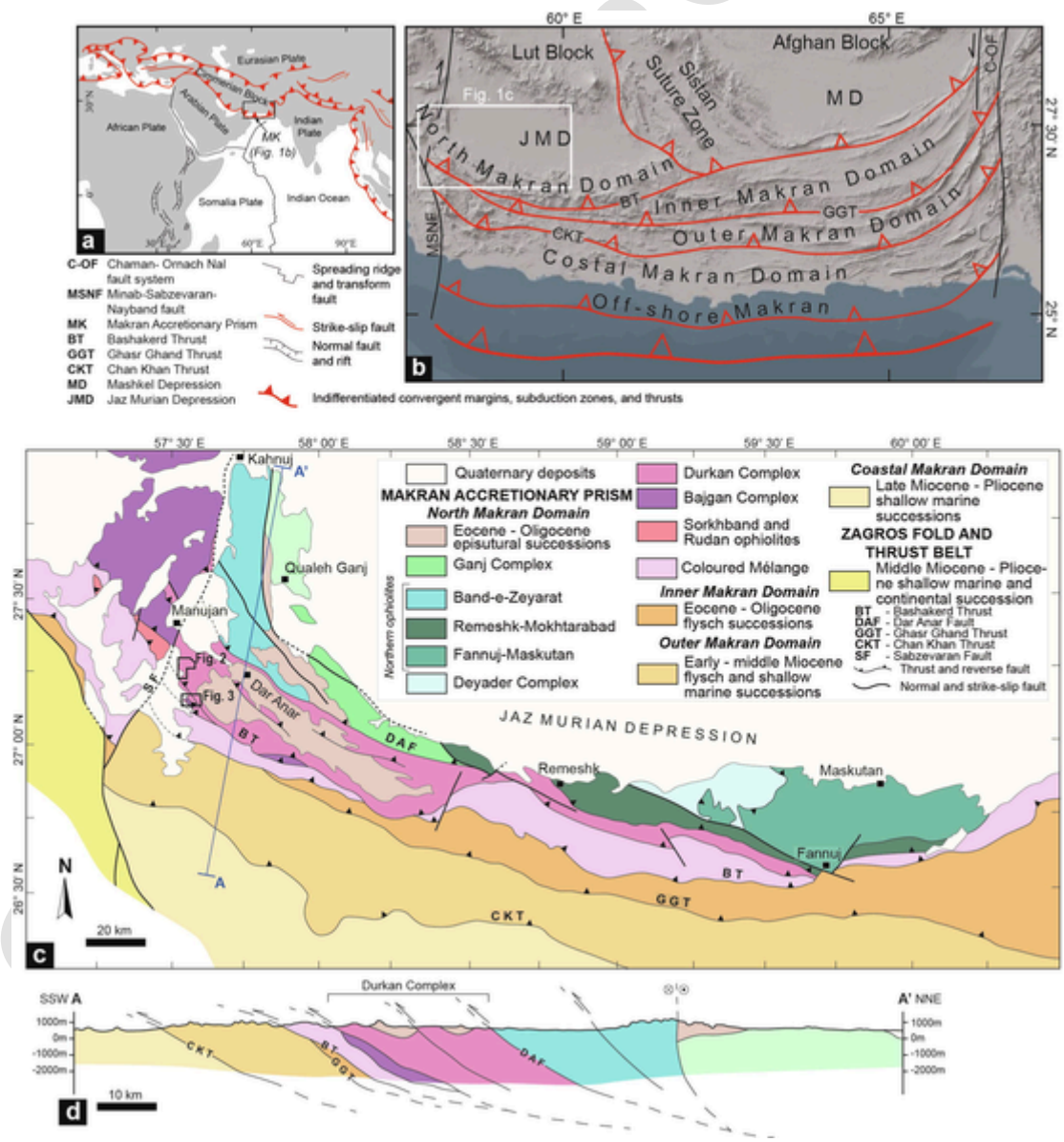

Fig. 1. (a) Location of the Makran Accretionary Prism with respect to the Alpine-Himalayan orogenic belts (modified from Festa et al., 2018) showing the main tectonic plates; (b) simplified structural map of the Makran Accretionary Prism showing the different tectono-stratigraphic domains (from Burg et al., 2013); structural map (c) of the western Makran Accretionary Prism and geological cross-section (d) showing the tectonic units of the North Makran Domain (modified from Eftekhar-Nezhad et al., 1979; Samimi Namin, 1982, 1983; Burg, 2018; Barbero et al., 2021a).

standing of the mechanisms of seamounts accretion within convergent plate margins.

2. Regional geological setting

The Makran Accretionary Prism (hereafter Makran) is an E-W trending accretionary prism extending along strike for ~ 1000 km between the dextral Minab-Sabzevaran-Nayband and the sinistral Chamal-Ornach-Nal faults systems (Fig. 1a, b; McCall and Kidd, 1982; Burg et al., 2013; Burg, 2018; Haberland et al., 2021). This prism resulted from the convergence between Arabia and Eurasia resulted in the northward subduction of the NeoTethys oceanic lithosphere since the Cretaceous (Dercourt et al., 1986; Omrani et al., 2017; Barrier et al., 2018; Burg, 2018; Barbero et al., 2020a; Moghadam et al., 2022). The onshore Makran has been subdivided into four tectono-stratigraphic domains that are, from the structural top to the bottom, the North Makran, the Inner Makran, the Outer Makran, and the Coastal Makran (Fig. 1b; Dolati and Burg 2013; Burg, 2018). The North Makran is composed of several units (Fig. 1c, d) deformed at different depths within the accretionary prism during the Late Cretaceous – Paleocene (McCall, 2002; Omrani et al., 2017; Saccani et al., 2018, 2022a, Saccani et al., 2022b; Barbero et al., 2020b, Barbero et al., 2021a; Pandolfi et al., 2021; Esmaeili et al., 2022). This domain is separated from the Inner Makran by the Bashakerd Thrust, which represents a mainly E-W striking and N dipping thrust zone (Dolati, 2010; Burg et al., 2013; Burg, 2018). The Inner, Outer, and Coastal Makran domains progressively formed because of the incorporation of trench succession within the frontal wedge during the post-Eocene evolution of the accretionary prism (Platt et al., 1985; Burg et al., 2008, 2013; Mohammadi et al., 2016, Mohammadi et al., 2017).

The Durkan Complex is included in the North Makran domain, and it crops out from west to east for ~ 250 km (Fig. 1c). It includes an assemblage of tectonic slices, consisting of deformed stratigraphic successions, which are non-metamorphic or slightly metamorphic with a metamorphic overprint ranging from very low- to low-grade (McCall, 1985; Hunziker et al., 2015; Barbero et al., 2021a). The Durkan stratigraphic successions mainly consist of: (i) Upper Cretaceous - lower Paleocene shallow-water limestone associated with igneous rocks; (ii) alternation of pillow basalt, sandstone, shale, breccia, volcaniclastic rock, and chert; (iii) minor marble and schist (McCall, 1985, 2002; Barbero et al., 2021a). In addition, rare tectonic slices of Jurassic and Permian carbonate platform limestone have also been described (McCall, 1985, 2002). Hunziker et al (2015) have described in the eastern Durkan Complex an Early to Late Jurassic granitoid suite, intruding Jurassic shallow-water limestone. In the western Makran, Barbero et al. (2021a) distinguished three types of successions associated with transitional and alkaline basalts. Type-I consists of pillow basalt and volcaniclastic rock interbedded within a Coniacian - early Campanian pelagic succession of alternating chert, shale, marl, and cherty limestone. Type-II consists of a basal Cenomanian volcanic and volcaniclastic sequence followed by a pelagic and hemipelagic sequence. Both sequences are characterized by intercalations of mass-transport deposits suggesting volcanic activity and deposition in a slope setting (Barbero et al., 2021a). Type-III includes a volcanic sequence covered by a Cenomanian carbonate platform, in turn followed by a pelagic and hemipelagic sequence (Barbero et al., 2021a).

Given this complex tectono-stratigraphic architecture, different interpretations for the Durkan Complex have been so far proposed. In early studies, the Durkan Complex was interpreted as deformed remnants of a Permian - Paleocene sedimentary cover of a microcontinental block (the so-called Bajgan-Durkan microcontinent; see McCall and Kidd, 1982 for details). According to this view, the Bajgan Complex, which is formed by metamorphic assemblages interpreted as a Paleozoic continental basement was interpreted as the remnants of this continental block (McCall and Kidd, 1982; McCall, 1985). According to some geodynamic reconstructions, this continental block was detached from the southern Eurasia margin in response to a Middle – Late Jurassic rift (Hunziker et al., 2015; Burg, 2018). In contrast, recent multidisciplinary studies of the western Durkan Complex demonstrated that this complex mainly consists of remnants of a tectonically disrupted Late Cretaceous seamounts chain (Barbero et al., 2021a, Barbero et al., 2021b). These authors distinguished three stratigraphic successions. In detail, Type-I recorded pelagic sedimentation and volcanism during the deep-water stage of growth of a seamount; Type-II and Type-III resulted from sedimentation and volcanism within slope and cap of an emerged seamount, respectively. These interpretations are supported by new data on the Bajgan Complex, which demonstrated that it is composed of Jurassic – Cretaceous meta-ophiolite deformed at high pressure and low temperature conditions rather than remnants of the Bajgan-Durkan microcontinent (Pandolfi et al., 2021; Barbero et al., 2022).

3. Structural setting of the Durkan Complex in the western sector of the Makran

The Durkan Complex is bordered by the Dar-Anar Fault, to the north, and the Bashakerd Thrust, to the south (Fig. 1c, d). In the western Makran, this NW-SE striking thrust is crosscut by the NNE-striking dextral Sabzevaran Fault (Fig. 1c). In the next sections, we present multiscale structural data (from geological mapping to *meso*- and microscale structural analysis) from selected areas of the western Makran (Figs. 2 and 3; see Fig. 1c for area locations). For the stratigraphic architecture of the Durkan Complex, we follow the subdivisions into the Type-I, Type-II, and Type-III successions as proposed by Barbero et al. (2021a).

3.1. Lithostratigraphy and map-scale structural setting

The studied areas, namely Chah Shahi and Dehendar areas, are located in the hanging wall of the Bashakerd Thrust (Fig. 1c). Their map-scale structural setting is mainly influenced by this regional-scale thrust. In both areas NW- to NNW-striking and NE- to E-dipping thrusts juxtapose tectonic slices up to 1–2 km in thickness (Figs. 2 and 3a, b). These thrusts correspond to pluri-decametric fault zones that are characterized at the mesoscale by S—C shear zones. As shown by stereographic projection in Figs. 2c and 3c, the relationships between C and S planes indicate top-to-SW and -W thrusting. The stratigraphic successions in the different tectonic slices are deformed by two fold generations (Figs. 2b and 3b). In particular, the map-scale structural setting of the studied area is mainly influenced by kilometric sub-isoclinal and recumbent folds (Figs. 2b and 3b) formed during the D_1 deformation phase (see section 3.2.1).

3.1.1. The Chah Shahi area

In the northeast, different tectonic units (eastern units EU_1 and EU_2; Fig. 2a) are formed by Type-III stratigraphic successions showing abundant volcaniclastic rock within the volcanic and volcano-sedimentary sequences (Fig. 2a, b). These tectonic units are thrust westward onto tectonic units (i.e., central units CU_1 and CU_2, and western units WU_1 and WU_2; Fig. 2a, b) showing stratigraphic successions of Type-II, which are particularly rich of volcaniclastic rocks within the basal volcanic and volcano-sedimentary sequence. At different structural levels, lenticular and ~ 100 m thick slices of massive marble of the Type-III carbonate platform occur along the main thrusts (Fig. 2a). In the southern sector of Chah Shahi area, a km-thick unit composed of Type-I succession occurs between Type-II successions (southern unit SU1 and SU2; Fig. 2a). The stratigraphic succession of the tectonic unit SU2 is made up by a pelagic sequence showing pillow basalt interlayered with chert, cherty-limestone, and shaly marl. It is worth to note that the major thrust zones are preferentially localized within volcaniclastic se-

CORRECTED PROOF

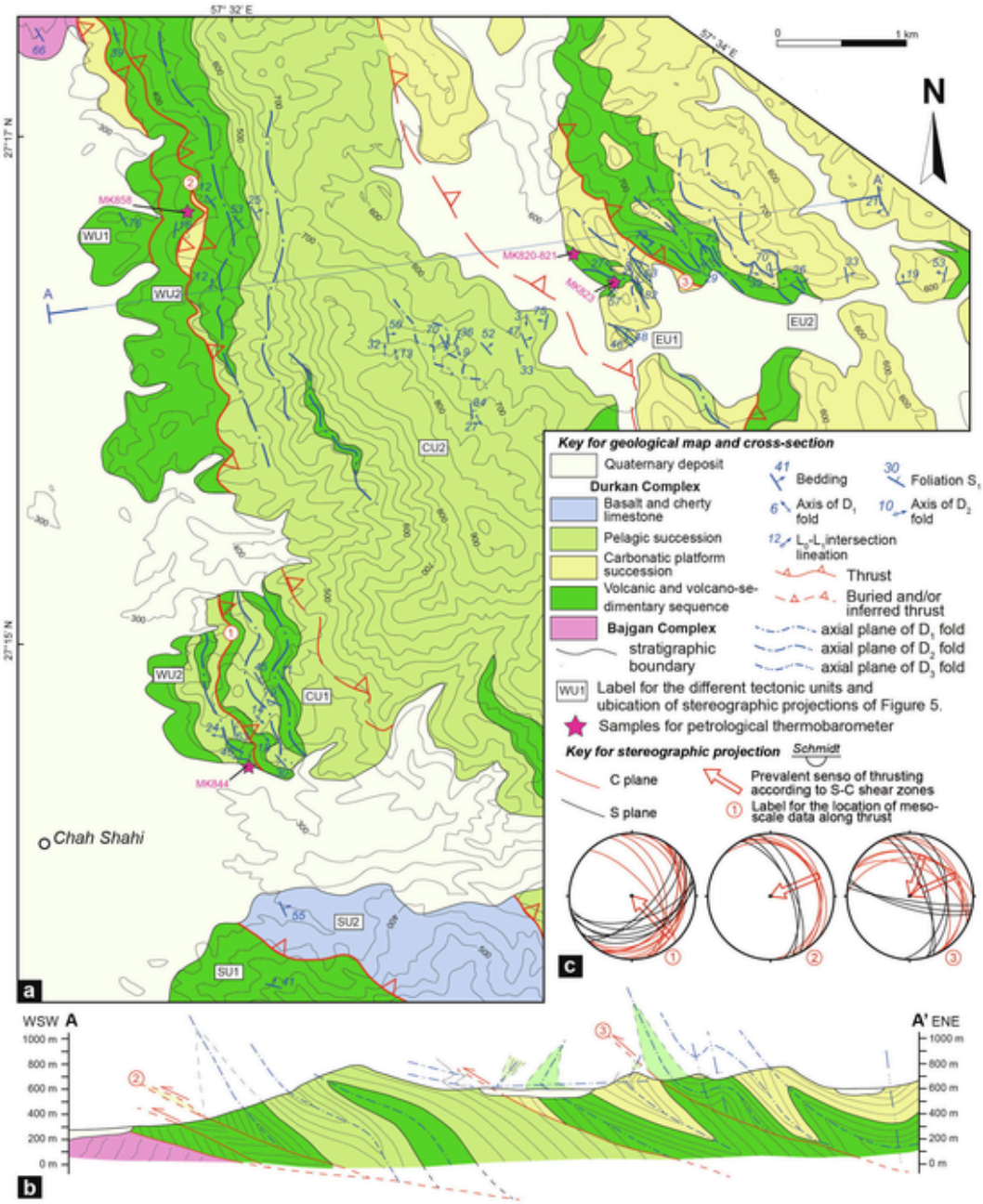

Fig. 2. (a) Simplified geological-structural map of the Durkan Complex in the Chah Shahi area (based on Samimi Namin, 1983 and modified according to our fieldwork and photointerpretation with satellite images) and related cross-section; (b) cross section showing the map-scale structural setting; (c) stereographic projections of the S—C shear zone along the main thrust zones shown in Panel (b). Labels indicate the different tectonic units. WU: Western Unit; EU: Eastern Unit; CU: Central Unit; SU: Southern Unit.

quence and commonly include lenticular tectonic slices of the Type-III carbonate platform sequence (Fig. 2a, b).

3.1.2. The Dehendar area

This area is located a few km to the east of the emergent tip of the Bashakerd Thrust (Fig. 1c). It is characterized by the juxtaposition of different tectonic units, whose successions belong to the Durkan Complex, the Bajgan Complex, and a Cenozoic siliciclastic turbiditic sequence (Fig. 3b). This sequence consists of centimetric to pluridecimetric beds of quartz-rich arenites alternated with shales and minor pluridecimetric beds of turbiditic limestone. Foraminifera biostratigraphy suggest a late Paleocene – Eocene age (see also McCall, 1985). In the Dehendar area, the Durkan Complex mainly crops out in two separated NNW-SSE trending belts, which occupy different structural positions within the tectonic stack of this area (Fig. 3a, b). The structurally uppermost belt is characterized by several tectonic units (i.e., the eastern units EU_1, EU_2, and EU_3 in Fig. 3a, b) juxtaposed by thrust zones. The stratigraphic succession of the tectonic units, as well as in the thrust zones is basically comparable to that of Type-II succession (Fig. 3a, b). In addition, massive marbles, platform limestones, and alkaline basalts commonly occur along the thrust zones separating the various tectonic units (Fig. 3a, b). The origin of limestones and marbles is enigmatic as these rocks do not show clear stratigraphic relationships with the other rocks and their fossils contents do not allow any age determination. However, they can be correlated with the carbonate platform sequence of the Type-III succession of the Durkan Complex based on

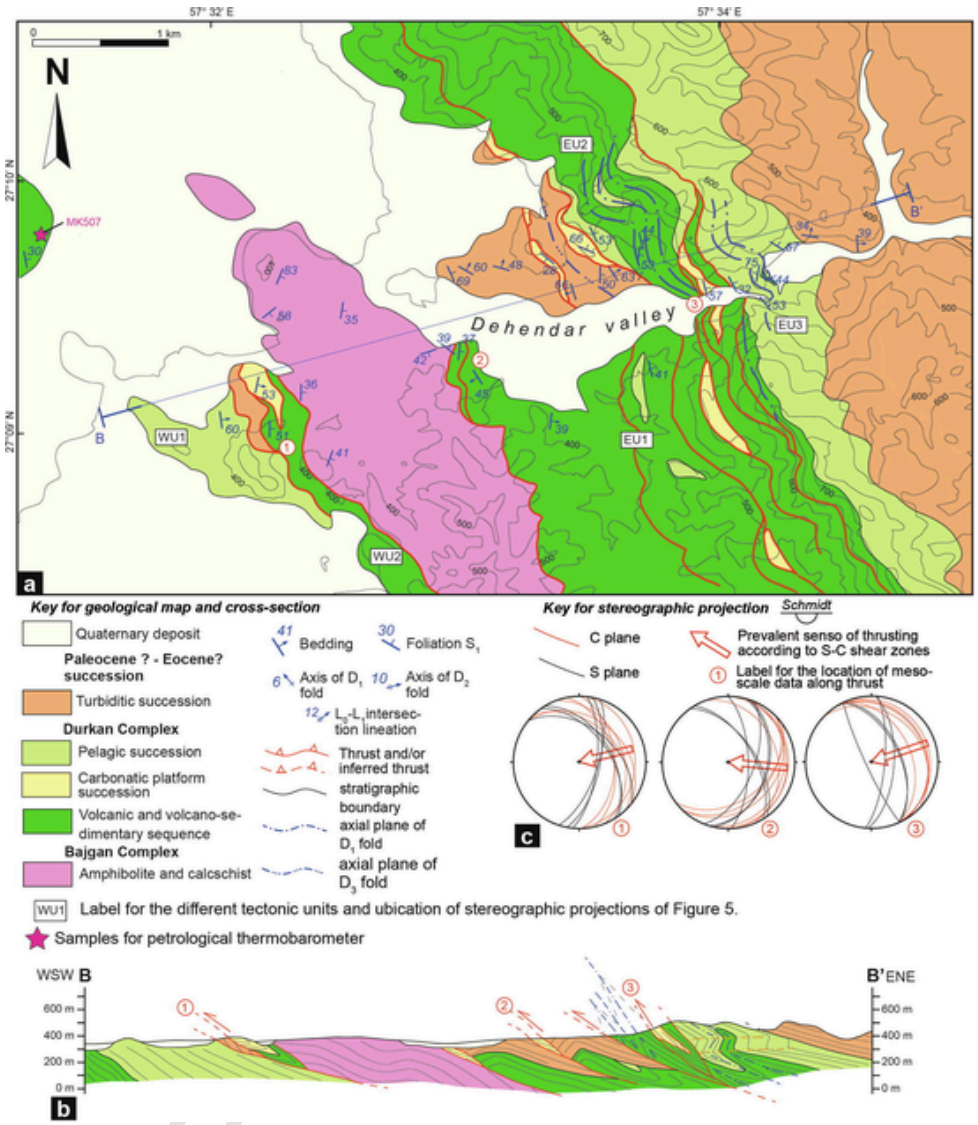

Fig. 3. (a) Simplified geological-structural map of the Durkan Complex in the Dehendar area (based on Samimi Namin, 1983 and modified according to our fieldwork and photointerpretation with satellite images) and (b) cross-section showing the map-scale structural setting; (c) stereographic projections of the S—C shear zone along the main thrust zones. Labels indicate the different tectonic units. WU: Western Unit; EU: Eastern Unit.

similar lithostratigraphic features, though another origin cannot be completely ruled out. Some tectonic units of the Durkan Complex (e.g., EU_1) are unconformably covered by upper Paleocene - Eocene turbiditic sequences (Fig. 3a, b). These units are thrust onto a tectonic unit of amphibolites and calcschists of the Bajgan Complex (Fig. 3a, b). The latter is thrust onto the structurally lowermost belt of the Durkan Complex, which is composed of two distinct tectonic units (i.e., WU_1 and WU_2, Fig. 3a, b). The upper unit (WU_2; Fig. 3a) includes a strongly foliated volcanic and a volcano-sedimentary sequence that can be correlated either with the Type-II or Type-III successions. The lower tectonic unit (WU_1; Fig. 3a) is composed of alternating cherty-limestone and shale, and a volcanic sequence of Type-II affinity (Fig. 3a, b). Along the thrust contact between WU_1 and WU_2, slices of massive marbles and a succession of alternating arenites are observed (Fig. 3a, b). The arenites are quartz-rich with foraminifera association of late Paleocene – Eocene age and represent the upper Paleocene – Eocene turbiditic sequence (see also McCall, 1985). Similar to the Chah Shahi area, tectonic slices of marbles and/or carbonate platform limestones occur along the major thrust zones that are preferentially developed within the volcaniclastic sequence of Type-II and/or Type-III successions (Fig. 3a, b). Finally, in the Dehendar area, a siliciclastic succession defines a relatively undeformed monocline gently dipping to E-NE (Fig. 3a, b). This succession rests on the composite structural stack with an erosional and angular unconformity (Fig. 3a, b). This succession includes arenites, conglomerates, as well as minor calcarenites, and it can be correlated with the Eocene succession resting unconformably onto the North Makran units (the Marich Unit of McCall, 1985). Additional biostratigraphic studies are needed to better constraint its depositional age, and consequently, the timing of the deformation of the Durkan Complex.

3.2. *Deformation history of the western Durkan Complex*

The new schematic geological maps (Figs. 2a and 3a) and the *meso-* and micro-scale structural analysis performed in the studied area allowed us to recognize three deformative phases, namely the D_1, D_2, and D_3 phases.

3.2.1. *D_1 phase*

The D_1 deformation phase is associated with macro- to micro-scale asymmetric folds, which are non-cylindrical similar folds (Ramsay, 1967), ranging from sub-isoclinal to close (Fig. 4a, b). They are characterized by thickened and generally rounded hinge zones, as well as

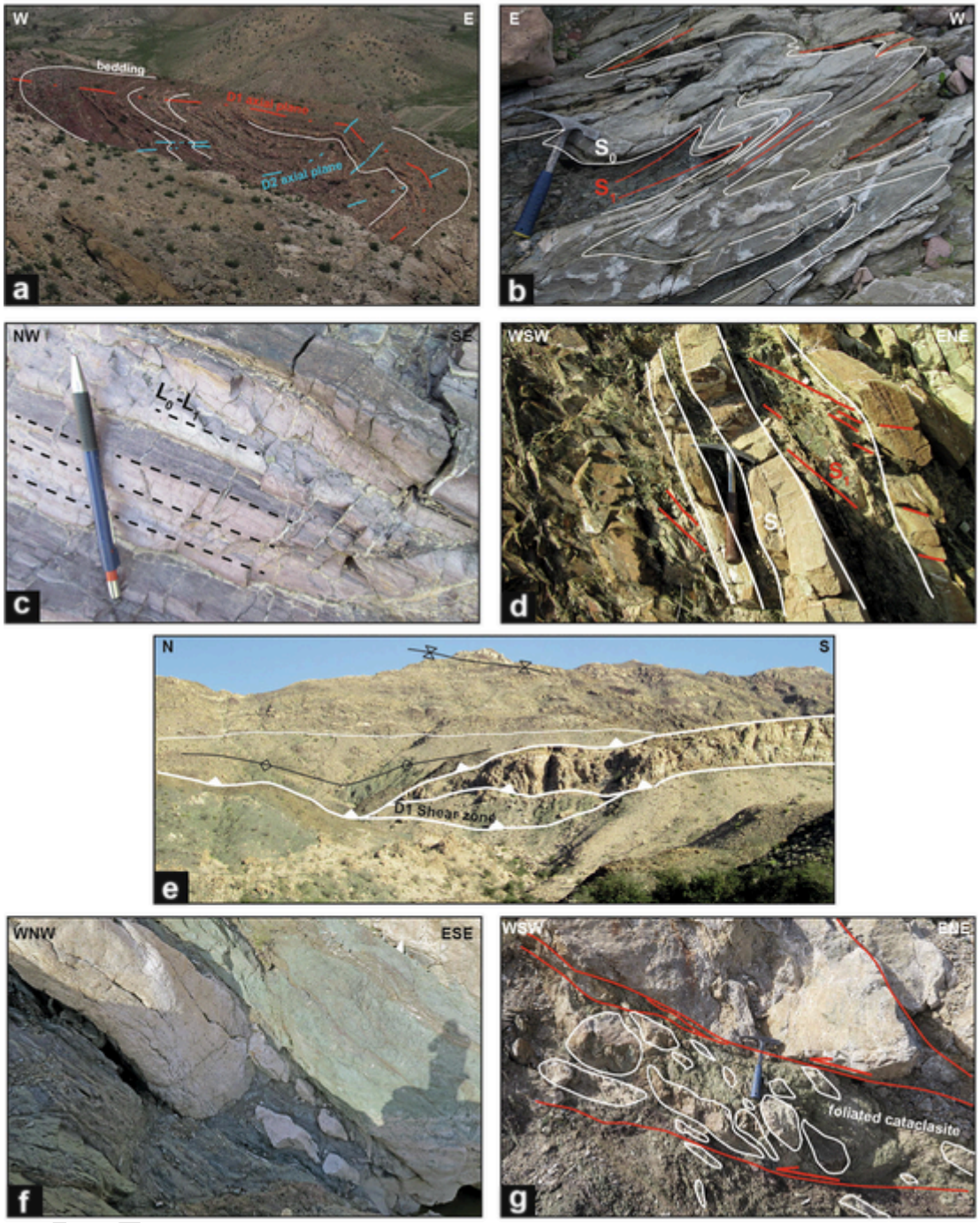

Fig. 4. Field occurrences of the D_1 deformation phase recognized in the Durkan Complex: (a) macroscopic W-verging D_1 anticline re-folded by E-verging D_2 folds; (b) mesoscopic D_1 sub-isoclinal folds within alternating *meta*-limestone and shale (white and red lines indicate the bedding S_0 and S_1 foliation, respectively); (c) vari-coloured shale showing intersection lineation between bedding S_0 and S_1 foliation (L_0-L_1); d) relationship between bedding S_0 (white line) and foliation S_1 (red line) in alternating meta-limestone and shale along an overturned limb of D_1 anticline; (e) panoramic view of the D_1 shear zone along overturned limb of a macroscopic W-verging D_1 anticline. Black arrows indicate the polarity of the succession. White line and black line indicate thrust fault and trace of fold axial plane, respectively; (f) mesoscopic features of the D_1 shear zones showing up to metric-thick blocks of whitish marble within a foliated matrix composed of cataclasites derived from volcaniclastic rocks; (g) close-up of the D_1 shear zones showing block-in-matrix fabric with foliated cataclasite and anastomosed faults enclosing and bounding marble and meta-basalt blocks (red line and white line represent fault and boundary of the blocks, respectively). (For interpretation of the references to colour in this figure legend, the reader is referred to the web version of this article.)

stretched and thinned limbs (Fig. 4b) locally affected by boudinage of the competent beds. In some tectonic slices (in the Chah Shahi WU_1, WU_2, and EU_1, see Fig. 2a; in the Dehendar EU_2, see Fig. 3a), the folds are more pervasive at the mesoscale, isoclinal to sub-isoclinal, and characterized by significant stretching of the overturned limb (Fig. 4b). The D_1 folds are associated with an axial-plane foliation S_1 sub-parallel or at low angle to the S_0 bedding (Fig. 4b and 5). The S_1 foliation is well developed in all the lithotypes (see section 4) and produces an intersection lineation with the S_0 bedding (i.e., L_0-L_1), which is represented by either a marked colour variation along the foliation surface in shales (Fig. 4c) or mullion structures where more competent beds are abundant. The L_0-L_1 lineation is parallel to the fold axes (Fig. 5). In the slices

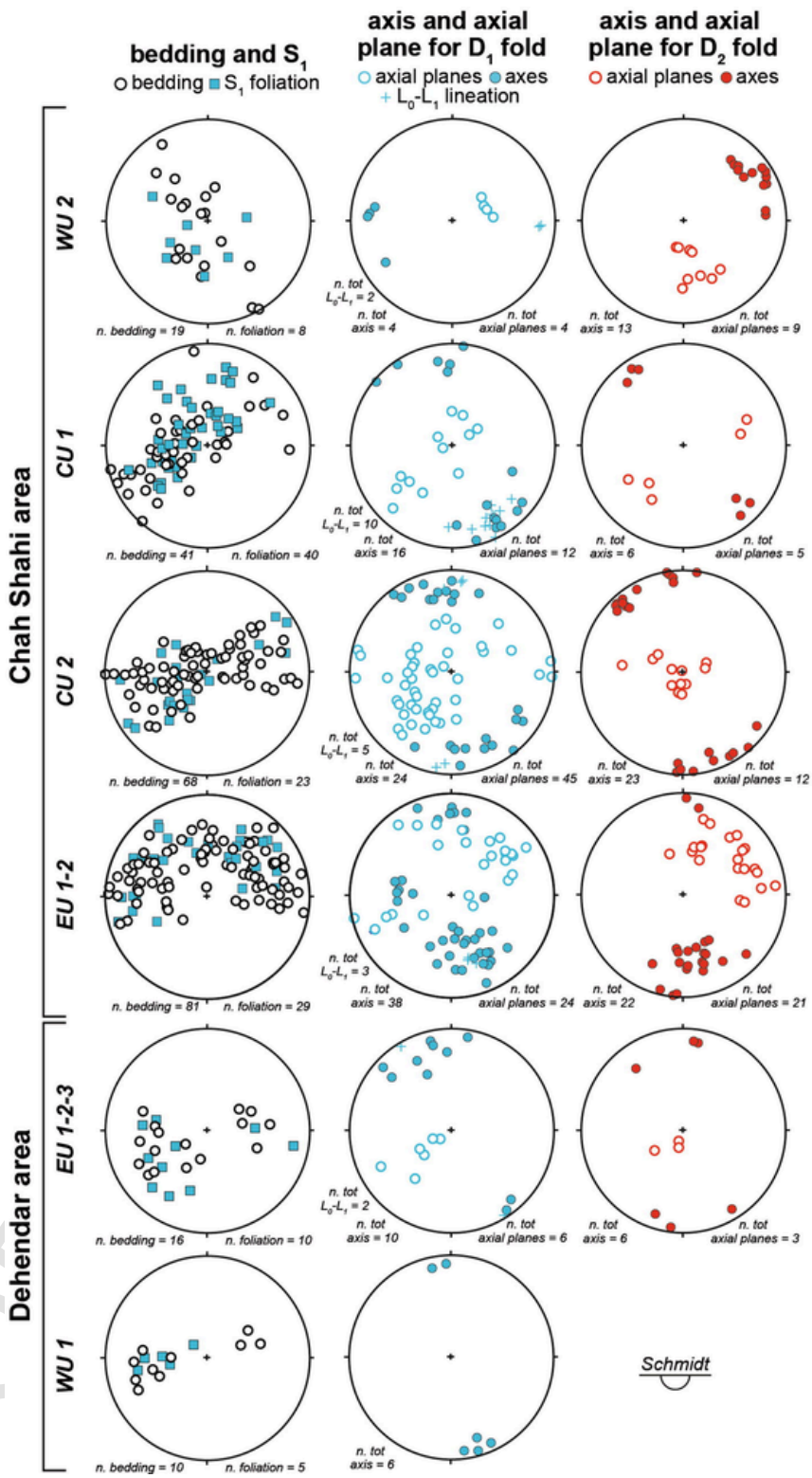

Fig. 5. Stereographic projections (equal area, lower hemisphere) of the structural elements of D_1 and D_2 phases for the different tectonic units in the Chah Shahi and Dehendar areas (labels and locations of each unit are reported in Figs. 2 and 3). Planar structural elements are plotted as pole to plane. WU: Western Unit; EU: Eastern Unit; CU: Central Unit.

showing pervasive meso-scale folding deformation, the foliation is well developed in all the lithotype from the meta-basalts to the marble and shale (see section 4). By contrast, in the units with less pervasive folding (in the Chah Shahi CU_1, CU_2, and EU_2, see Fig. 2a; in the Dehendar WU_1, WU_2, EU_1, and EU_3 see Fig. 3a), the foliation shows different features based on the rock types at both *meso*- and micro-scale. In the shales, the S_1 foliation corresponds to a penetrative and mm-spaced slaty cleavage (Fig. 4d). In the meta-limestone and/or meta-volcaniclastic arenite, the S_1 foliation corresponds to a pressure solution cleavage. However, in the less deformed tectonic slices, the S_1 foli-

ation generally corresponds to a disjunctive cleavage preserved in the more competent meta-limestone and meta-arenite (Fig. 4d).

The D_1 folds show a general W-vergence and have sub-horizontal or slightly plunging axes trending mainly NW to NNW in most of the tectonic slices (Fig. 4a, b, Fig. 5). However, NE-SW orientation can locally be observed due to later deformation (Fig. 5). The axial planes are generally gently dipping toward NE (Fig. 5). The D_1 folds are locally associated with syn- to late-D_1 reverse shear zones generally developed along the overturned limbs of D_1 folds (Fig. 2a, b, Fig. 4e). These shear zones border the distinct tectonic units and show pluridecametric thickness. Internally, they correspond to strongly deformed zones showing a block-in-matrix fabric consisting of plurimetric to centimetric lens-shaped slices of meta-basalt and marble within a foliated matrix (Fig. 4f, g). The matrix is composed of foliated cataclasites preferentially formed from the deformation of volcaniclastic sequences (Fig. 4f) and it is characterized by shear bands and S—C structures (Fig. 4f, g). According to the geometry of shear bands and S—C structures, the shear zones show a general top-to-west sense of shearing and are locally folded by the D_2 folds. In the studied areas, the D_1 shear zones are commonly overprinted by brittle thrusting deformation associated with the D_3 phase.

3.2.2. D_2 phase

The D_2 deformation is characterized by heterogeneous folds from macro- to micro-scale; these folds are open to close and generally asymmetric (Fig. 4a and 6a, b) and deform the structural elements of the D_1 phase (Fig. 4a and 6c), providing thus relative chronological constraints for these two deformation phases. They generally show a parallel geometry. However, where the folded sequence shows an increase of the shale/competent beds (e.g., meta-arenite and meta-limestone) ratios, D_2 folds are similar with acute hinge zones. The superimposition on the folds and structural elements of D_1 phase produces a type 3 interference pattern (Ramsay, 1967) (Fig. 4a and 6c). The D_2 folds are associated with an axial plane foliation S_2 that is a disjunctive cleavage in the most competent beds and a crenulation cleavage in shales (Fig. 6b, c). It is worth to note that, differently from S_1 foliation, S_2 foliation is not associated with metamorphic recrystallization. The axial planes of D_2 folds are generally curviplanar and slightly inclined surfaces (Fig. 6c). Their orientations are different in the various tectonic slices, trending from NW-SE to W-E (Fig. 5). The axes of D_2 folds are generally sub-horizontal and show mainly NW-SE direction (Fig. 5). However, the trend of D_2 axes in some tectonic slices is N—S (Fig. 5), likely because of later deformation. The asymmetry of the folds indicates a NE- to E-vergence (Fig. 6b, c). Locally the D_2 folds are associated with low-angle and E-dipping extensional faults showing strike parallel to the D_2 fold axis and direction of movement to E-ENE.

3.2.3. D_3 phase

D_3 structures deform all the D_1 and D_2 structures of the Durkan Complex (Fig. 6d, e), as well as the upper Paleocene – Eocene turbiditic succession. D_3 deformation is characterized by W-verging thrust zones that are commonly responsible for the map-scale juxtaposition of the different units. At the *meso*-scale, the D_3 thrust zones are characterized by brittle deformation localized along discrete fault planes showing S—C deformation zones (Fig. 6e). The D_3 thrusts zones are locally associated with meso-to macro-scale ramp folds (Fig. 6f). These folds are open to close, and asymmetric, showing a sub-vertical to rather inclined axial plane, sub-horizontal axis (Fig. 6f), and they are not associated with an axial plane foliation.

4. Features of syn-D_1 metamorphism

4.1. S_1 foliation in the different lithologies: Petrography and mineral chemistry

4.1.1. Petrography

As shown in the previous section, the S_1 axial plane foliation relating to the D_1 folds shows different features and dynamic recrystallization depending on the rock type. In this section, we will briefly describe the microstructural features (Fig. 7) and the mineralogy (Fig. 8) of the S_1 foliation in the different rock types, as these data are the starting point for the pressure–temperature (*P-T*) estimates for the D_1 tectono-metamorphic event (see section 4.2 and Supplementary Data S1).

In the meta-basalts (samples MK823 and MK507), the S_1 foliation is heterogeneously developed. In sample MK507 the volcanic texture is still well recognizable with clinopyroxene porphyroclasts set in a fine-grain matrix (Fig. 7a, b). The S_1 foliation is weakly developed, and it is defined by an aggregate of chlorite, fine-grained amphibole, and epidote (Fig. 7b). In sample MK823 the metamorphic recrystallization almost completely overprinted the volcanic texture. In this case, the S_1 foliation is defined by the alternation of fine- to medium-grained aggregate of chlorite + muscovite and lenticular aggregates of fine-grained albite (Fig. 7c). In addition, less abundant epidote and amphibole grow along the foliation (Fig. 7c). Finally, rare titanite occur in the S_1 foliation as well (Fig. 7c). The S_1 foliation wraps porphyroclasts of magmatic clinopyroxene that were, in turn, re-oriented along the foliation. These porphyroclasts are in some cases pseudomorphosed by epidote and/or amphibole.

The meta-volcaniclastic rocks range from meta-volcaniclastic arenites to meta-volcaniclastic breccias. In meta-volcaniclastic arenites (samples MK820 and MK821), the S_1 foliation is a millimetric-spaced planar fabric defined by the alternation of mineralogically different domains (Fig. 7d). In detail, aggregates of chlorite and white mica define a clear planar anisotropy (Fig. 7e). These domains alternate with lens-shaped domains composed of fine- to medium-grained aggregates of calcite, quartz, and albite, with subordinate chlorite and white mica (Fig. 7d). In the samples from the slightly metamorphosed tectonic slices, the S_1 foliation is characterized by isooriented calcite grains together with very fine-grained and indistinguishable phyllosilicates and clay minerals. In the meta-volcaniclastic breccias (samples MK844 and MK858) the S_1 foliation is less continuous, wrapping around volcanic clasts and/or detrital individual crystals (mainly clinopyroxenes), and it is well developed in the pressure shadows of the pre-existing clasts. The foliation includes aggregates of isooriented calcite and albite grains and minor quartz, as well as chlorite and white mica (Fig. 7f). Calcite, albite, and quartz aggregates generally shows crystallographic preferential orientation.

In the meta-sedimentary rocks, the S_1 foliation is well developed in the carbonate rocks, which include marble and impure marble. In the marble, the foliation is defined by isooriented calcite grains, ranging from fine- to medium-grained and rare white mica, chlorite, and quartz. The impure marble differs from the marble for a greater abundance of phyllosilicate phases (chlorite and white mica) and quartz; it also shows the occurrence of dissolutions seems of reddish to brownish clay minerals (Fig. 7g). In the shales, the very fine grain makes difficult the recognition of the mineral assemblages. However, in some cases the S_1 foliation is a slaty cleavage defined by clay minerals and less abundant quartz and calcite.

Finally, the S_1 foliation is folded by open and generally asymmetric micro-scale folds corresponding to the D_2 phase (Fig. 7h). The overprinting relationship is well identified at the micro-scale within the fine-grained *meta*-volcaniclastic rocks (Fig. 7h). The D_2 folds are not associated with metamorphic recrystallization; by contrast they are associated to a S_2 disjunctive cleavage marked by either the localized re-

UNCORRECTED PROOF

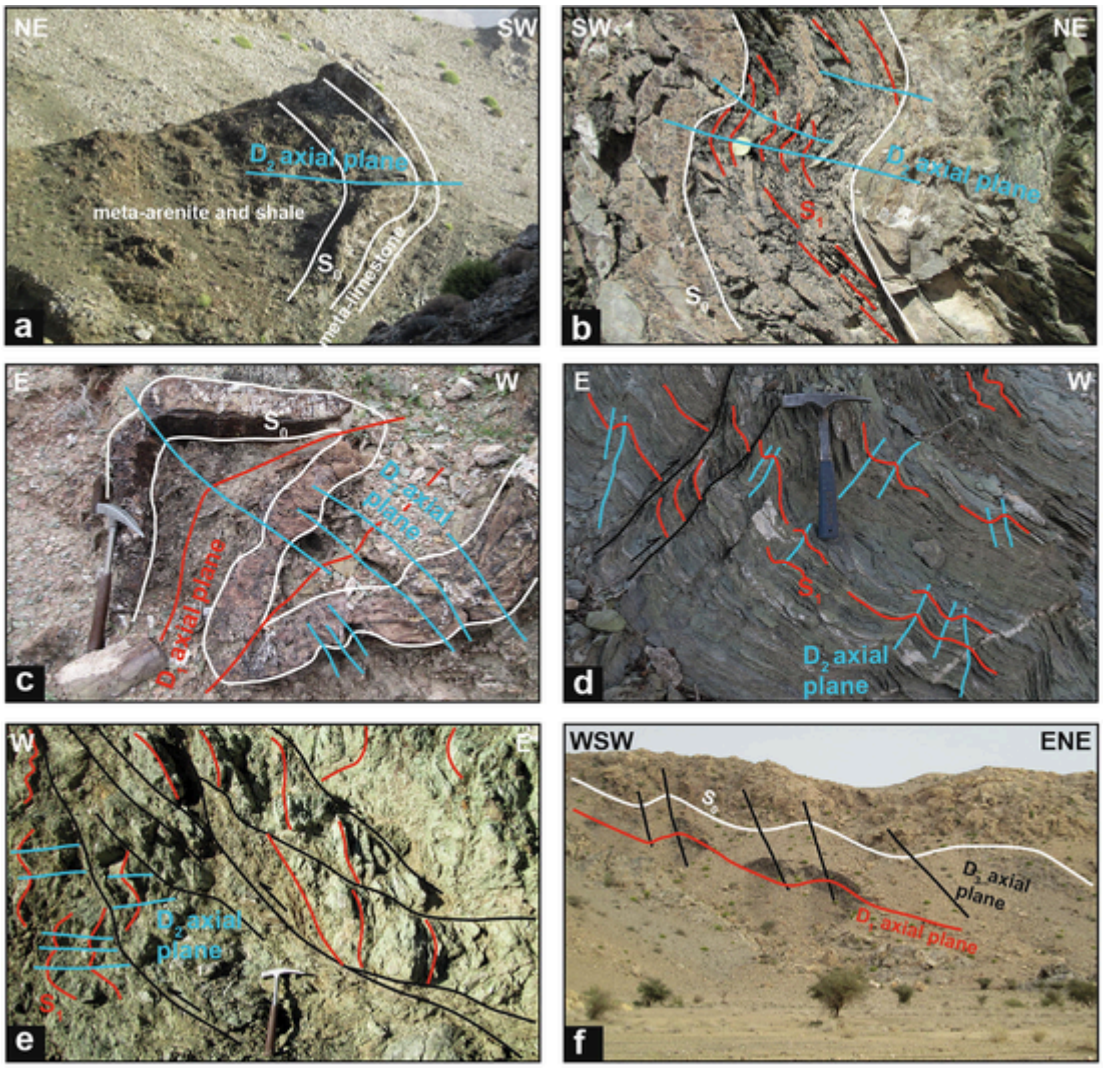

Fig. 6. Field occurrences of the D_2 (a-c) and D_3 (d-f) deformation phases recognized in the Durkan Complex: (a) macro-scale open fold (light blue line indicate axial plane) deforming stratigraphic alternation (white line) of *meta*-limestone and volcaniclastic *meta*-arenites and shales; (b) close-up of asymmetric NE-verging open folds deforming primary stratigraphic alternation of *meta*-limestone and shale (white line) as well as S_1 foliation (red line) in the shale; (c) *meso*-scale occurrence of type 3 interference pattern between D_1 and D_2 folds (red lines: D_1 axial plane; light blue lines: D_2 axial plane; white lines: bedding); (d) *meso*-scale relative chronological relationships between deformations phases: W-verging reverse faults (black lines) crosscut D_2 E-verging crenulation folds (light blue lines represent axial planes) that, in turn, deform the S_1 foliation (red lines); (e) *meso*-scale W-verging thrust zone showing S—C structure (black and red lines indicate C and S planes, respectively) crosscutting structural elements of D_1 and D_2 folds (red line: S_1 foliation; light blue line: D_2 axial plane); (f) macro-scale open D_3 folds deforming normal flank of macro-scale D_1 anticline (white line: bedding S_0; red line: S_1 axial plane; black line: D_3 axial plane). (For interpretation of the references to colour in this figure legend, the reader is referred to the web version of this article.)

orientation of phyllosilicates (e.g., chlorite) of the S_1 foliation or microfaults along the hinges zone (Fig. 7h).

4.1.2. Mineral chemistry of S_1 foliation in meta-basalts and meta-volcaniclastic rocks

To characterize the D_1 metamorphic condition, major element mineral chemistry of chlorite, white mica, and amphibole recrystallized within the S_1 foliation was determined on selected samples of *meta*-basalts and *meta*-volcaniclastic rocks. Detail of methods and analytical conditions are given in the Supplementary Data S1. Representative analyses are shown in Tables 1-3, whereas the complete dataset is shown in the Supplementary Data S2.

In the *meta*-basalts (samples MK823 and MK507), chlorite composition is characterized by Al_{tot} (Al^{IV} + Al^{VI}) content ranging from 1.90 to 2.40 a.p.f.u., Si content between 2.85 and 3.00 and X_{Mg} (=Mg/(Mg + Fe^{2+})) between 0.50 and 0.60 (Fig. 9a, Table 1). A slight chemical difference can be seen among samples from different tectonic units (Fig. 9a and Fig. 2a, 3b for location of the different units). The (FeO + MgO)/SiO_2 proportion indicates their affinity with clinochlore/daphnite endmembers (80 %-95 %) with minor miscibility with amesite and minor sudoite (Fig. 9a). White mica was only found in sample MK823. It is characterized by Si and Al contents of 3.40–3.60 and 1.60–2.10 a.p.f.u., respectively. The K content is higher than 0.70 a.p.f.u. (Table 2). Their composition is predominantly that of muscovitic celadonite (40 %-70 % of celadonite) due to activation of Tschermak substitution, with minor tendency to muscovite (Fig. 9b). Amphibole occurs in the *meta*-basalts sampled in the tectonic units EU_1 (MK823, Fig. 2a) and WU_1 (MK507, Fig. 3a). They are mostly calcic (actinolite) and subordinately calcic-sodic (winchite) amphiboles (Leake et al., 1997; Table 3).

In *meta*-volcaniclastic rocks (MK844, MK858, MK820 and MK821 samples), chlorite has Si content between 2.65 and 3.00 a.p.f.u. (Fig. 9a). Al in chlorite strongly varies from sample to sample, as well as X_{Mg}, which tends to be higher than 0.60. The typicality of the samples is re-

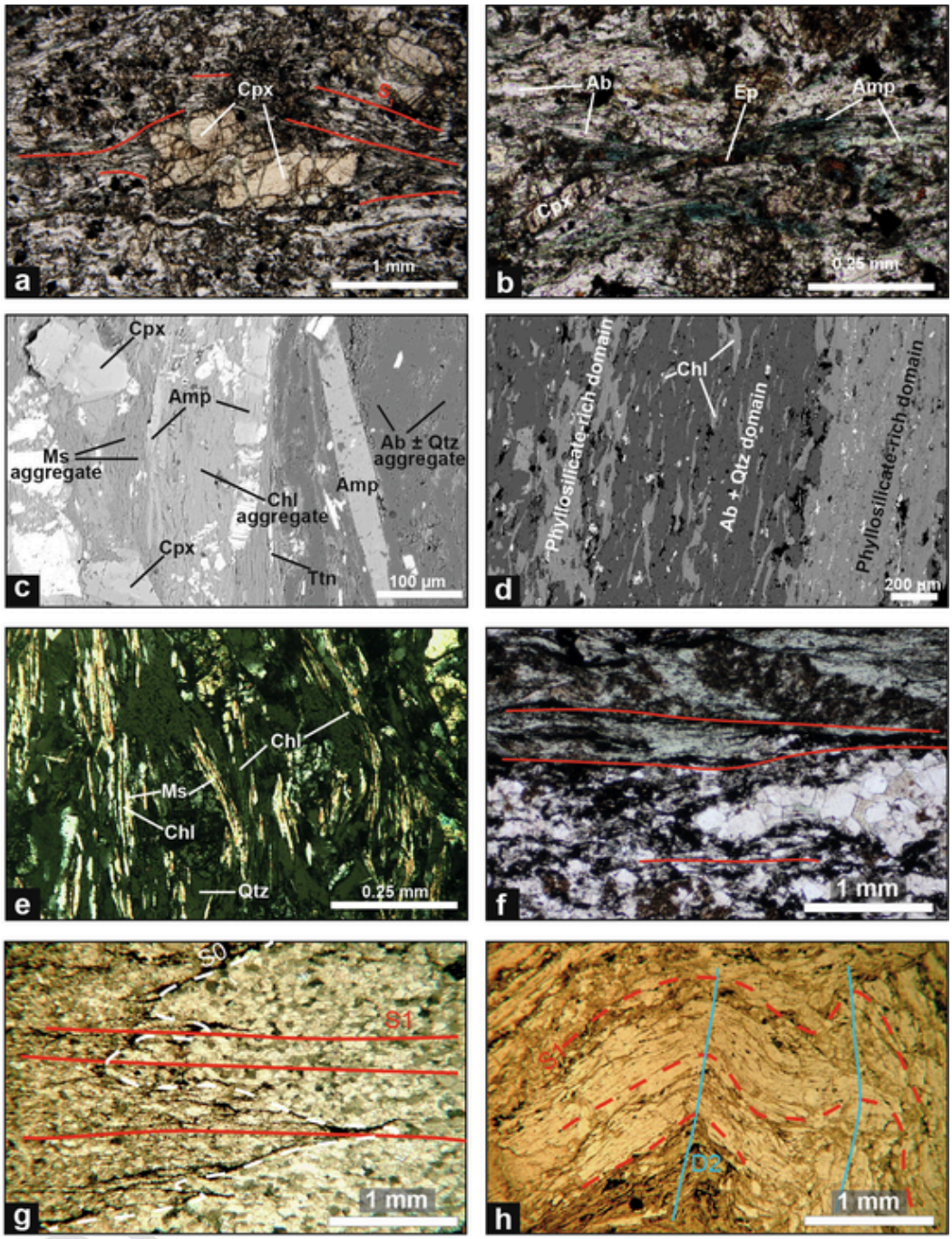

Fig. 7. Photomicrographs of microstructures of the D_1 phase recognized in the Durkan Complex (abbreviations: Ab: albite; Amp: amphibole; Chl: chlorite; Cpx: clinopyroxene; Ep: epidote; Ms: muscovite; Qtz: quartz; Ti: titanite); (a) relict of a magmatic clinopyroxene surrounded by the fine-grained S_1 foliation (red line) in *meta*-basalt; (b) detail of the metamorphic S_1 foliation defined by amphibole, epidote, and minor albite in *meta*-basalt; (c-d) back scattered electron (BSE) images showing the textural feature of S_1 foliation in *meta*-basalt (c) and *meta*-volcaniclastic arenite (d). The foliation in the *meta*-basalt wraps around zoned magmatic clinopyroxene and it is defined by aggregate of albite and quartz, aggregate of chlorite and white mica, as well as amphibole, and rare titanite. The foliation in the *meta*-volcaniclastic arenite is defined by the alteration of phyllosilicate-rich and albite-quartz-rich domains; (e) texture and mineralogical composition of the S_1 foliation in *meta*-volcaniclastic arenite. S_1 foliation is mainly defined by the isooriented chlorite and white mica; (f) feature of the S_1 foliation in volcaniclastic rock. S_1 is defined by an aggregate of quartz and albite alternating with chlorite and clay minerals bands; (g) D_1 microfolds deforming a stratigraphic alternation (S_0 in figures, white dashed line) of coarse-grained *meta*-limestone and fine-grained *meta*-impure limestone. S_1 foliation (red line) is defined by elongated calcite grains and dissolution seems; (h) photomicrographs showing S_1 foliation (red dashed line) in volcaniclastic rock deformed by D_2 microfolds (light blue line indicate fold axial planes). D_2 folds produce a weak reorientation of the phyllosilicates of the S_1 foliation. (For interpretation of the references to colour in this figure legend, the reader is referred to the web version of this article.)

flected on end-member affinities: in the tectonic unit WU_2 (Fig. 2a), chlorite crystals of sample MK858 have the structural formula close to pure clinochlore/daphnite, whereas those of samples MK844, MK820, and MK821 are mixed with amesite and minor sudoite (Fig. 9a). White mica is characterized by Al content ranging between 1.60 and 1.80 a.p.f.u. in MK858, 1.50–2.20 in MK820 and MK821 and 1.50–2.30 a.p.f.u. in MK844, whereas Si content strongly varies in samples of WU (MK858 and MK844) from those of EU (MK820 and MK821, Fig. 9b). K

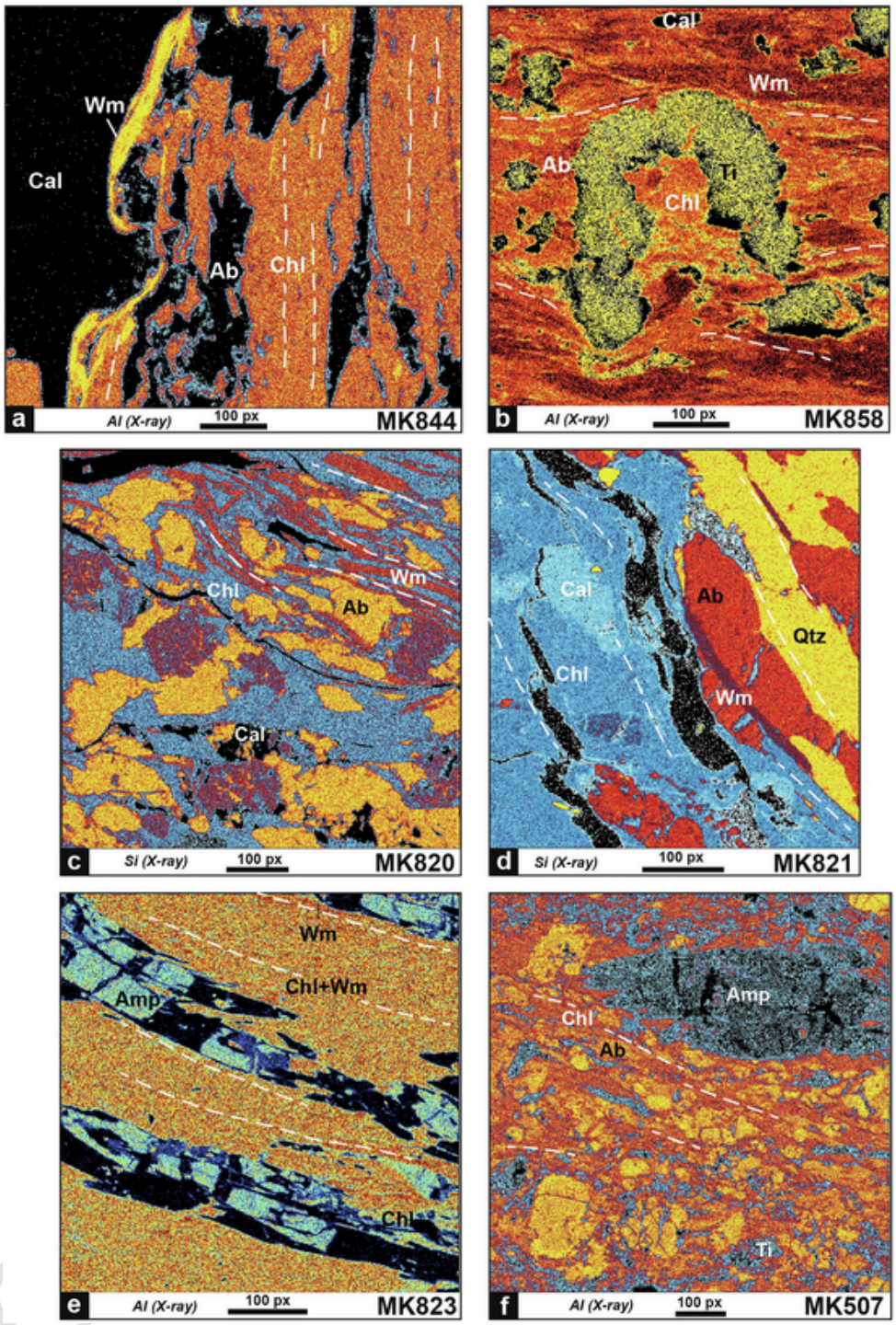

Fig. 8. micro-photographs acquired with the microprobe showing the S_1 foliation (withe dashed lines) in the studied samples. (Abbreviations: Ab: albite; Amp: amphibole; Cal: calcite; Chl: chlorite; Qtz: quartz; Ti: titanite; Wm: white mica). (a) Al intensity map of sample MK844; (b) Al intensity map of sample MK858; (c) Si intensity map of sample MK820; (d) Si intensity map of sample MK821; (e) Al intensity map of sample MK823 and (f) Al intensity map of sample MK507.

in white mica ranges between 0.50 and 1 in almost all the samples except for MK844 in which vary from 0.70 and 1.00. The end-members are expressed in different proportions into the samples, making the white mica of the samples MK858, MK844 and MK820 muscovitic celadonites and those of the sample MK821 muscovites with minor celadonite (Fig. 9b). Analyses with sum of oxide too low with respect to typical end-member or with mixed chlorite-phengite compositions were not used for thermobarometric estimation.

4.2. Estimation of the P-T conditions during the D_1 phase

Different methods have been applied to estimate the *P-T* conditions during the D_1 tectono-metamorphic evolution of the Durkan Complex. In detail, *P-T* conditions on *meta*-basaltic and *meta*-volcaniclastic rocks were estimated by crossing the results obtained from petrological geothermobarometers based on chlorite and white mica compositions. The detailed description of the methods used is given in Supplementary Data S1. All the calculations were performed setting the water activity

Table 1
Representative electron microprobe analyses of chlorites from the Durkan Complex. Calculation of atoms per formula unit (a.p.f.u.) is based on 14 oxygen.

Locality - unit	Chah Shahi – western unit						Chah Shahi – eastern unit									Dehendar		
Sample	MK844			MK858			MK820			MK821			MK823			MK507		
Mineral	*1*	*10*	*9*	*1*	*3*	*6*	*2*	*5*	*7*	*2*	*3*	*7*	*4*	*6*	*9*	*2*	*4*	*8*
wt.%																		
SiO_2	27.43	27.20	30.51	29.64	29.79	28.61	28.34	28.60	29.26	28.32	27.72	29.02	29.46	28.92	28.69	27.47	28.17	28.25
TiO_2	b.d.l.	0.02	0.06	0.11	0.05	0.12	0.01	0.03	0.03	0.08	b.d.l.	0.06	0.06	0.07	0.13	0.06	0.02	0.02
Al_2O_3	21.87	22.14	22.32	17.68	17.41	16.24	19.25	20.14	19.29	20.30	20.48	20.28	16.79	18.20	18.83	17.94	17.72	17.89
FeO	18.20	18.88	17.42	13.01	12.59	16.01	18.69	17.96	18.98	18.76	20.43	19.32	25.49	25.63	26.00	26.09	26.13	26.25
MnO	0.04	0.05	0.08	b.d.l.	0.06	0.12	0.29	0.26	0.38	0.29	0.26	0.27	0.46	0.45	0.44	0.54	0.51	0.53
MgO	20.23	19.03	17.00	25.98	26.89	24.88	21.77	21.94	20.44	20.62	19.72	19.98	17.86	17.06	17.48	16.79	16.42	16.85
CaO	0.11	0.22	0.43	0.22	0.08	0.39	0.03	0.08	0.07	0.07	0.15	0.09	0.08	0.13	0.12	0.09	0.14	0.11
Na_2O	0.02	0.02	0.02	0.06	0.04	0.06	b.d.l.	0.03	0.04	0.04	0.04	b.d.l.	0.03	0.06	b.d.l.	0.01	b.d.l.	0.03
K_2O	0.01	0.02	1.00	0.01	0.02	0.04	b.d.l.	0.01	0.03	0.03	b.d.l.	0.04	0.04	0.05	0.10	0.03	0.05	0.01
Total	87.92	87.60	88.84	86.72	86.92	86.46	88.39	89.05	88.53	88.51	88.80	89.06	90.26	90.57	91.79	89.02	89.15	89.93
a.p.f.u.																		
Si	2.761	2.758	3.015	2.951	2.953	2.920	2.852	2.841	2.937	2.843	2.801	2.896	3.007	2.942	2.885	2.866	2.929	2.912
Al ^{IV}	1.239	1.242	0.985	1.049	1.047	1.080	1.148	1.159	1.063	1.157	1.199	1.104	0.993	1.058	1.115	1.134	1.071	1.088
Al ^{VI}	1.356	1.404	1.615	1.025	0.978	0.873	1.136	1.200	1.219	1.245	1.240	1.282	1.027	1.125	1.116	1.072	1.101	1.085
Ti	0.000	0.002	0.005	0.009	0.004	0.009	0.001	0.002	0.003	0.006	0.000	0.004	0.005	0.006	0.010	0.005	0.001	0.001
Fe^{2+}	1.532	1.601	1.440	1.083	1.044	1.366	1.573	1.492	1.593	1.575	1.726	1.613	2.176	2.181	2.186	2.277	2.272	2.263
Mn	0.004	0.004	0.007	0.000	0.005	0.010	0.025	0.022	0.033	0.024	0.022	0.023	0.039	0.039	0.038	0.047	0.045	0.046
Mg	3.036	2.877	2.505	3.856	3.974	3.785	3.267	3.249	3.058	3.086	2.970	2.973	2.718	2.588	2.620	2.612	2.546	2.589
Ca	0.012	0.024	0.045	0.024	0.008	0.042	0.004	0.008	0.008	0.008	0.016	0.010	0.009	0.014	0.013	0.010	0.015	0.012
Na	0.004	0.005	0.004	0.011	0.007	0.011	0.000	0.006	0.008	0.008	0.008	0.000	0.005	0.013	0.000	0.003	0.000	0.005
K	0.002	0.003	0.126	0.002	0.003	0.005	0.000	0.002	0.004	0.004	0.000	0.005	0.005	0.007	0.013	0.003	0.006	0.002
Total	9.944	9.921	9.745	10.010	10.031	10.103	10.005	9.981	9.925	9.956	9.984	9.909	9.983	9.970	9.996	10.029	9.986	10.003
X_{Mg}	0.665	0.642	0.635	0.781	0.792	0.735	0.675	0.685	0.657	0.662	0.632	0.648	0.555	0.543	0.545	0.534	0.528	0.534

Note: X_{Mg} = Mg / (Mg + Fe^{2+}); b.d.l. – below detection limits.

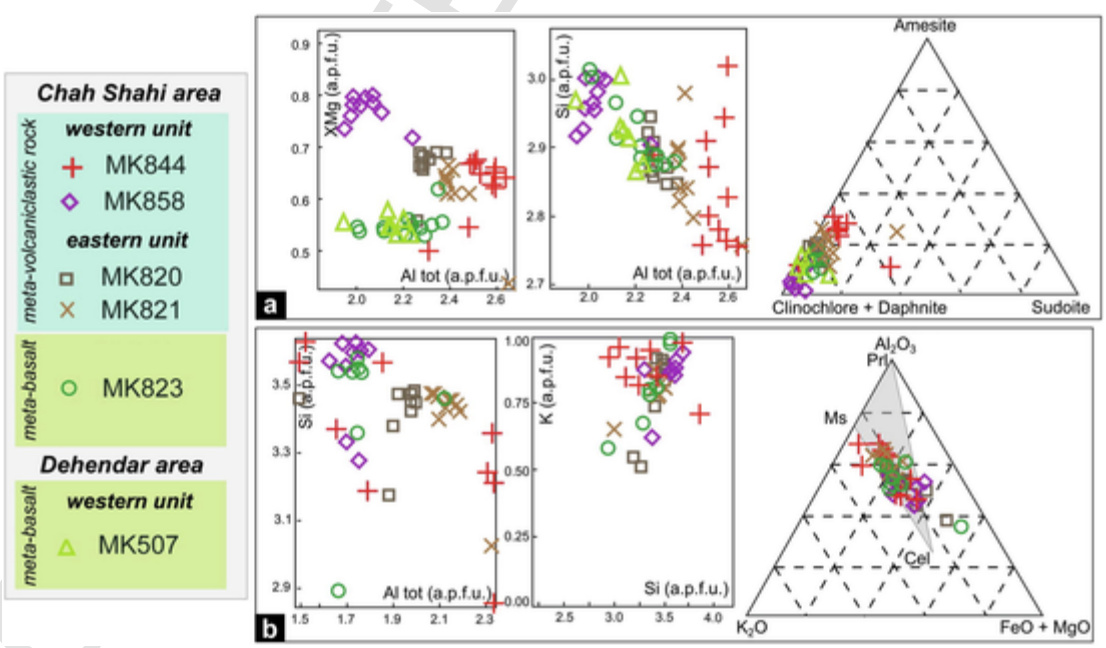

Fig. 9. Chemistry of (a) chlorite and (b) white mica of samples studied in this work (the whole dataset of analyses used for this figure is shown in Supplementary Data S2). The locations and labels of the tectonic units where the samples have been collected and the locations of the samples for geothermobarometric investigations are shown in the Fig. 2a and 3a.

to 0.8 because all the samples contain calcite (see Di Rosa et al., 2020a, 2020b; Frassi et al., 2022).

Temperature conditions were calculated with the chlorite-quartz-water method (Vidal et al., 2006) on all the samples from Chah Shahi and Dehendar areas. Calculations were performed fixing 4 different pressure values (0.7, 0.8, 0.9 and 1.0 GPa; see Supplementary Data S1). We considered the best fit (i.e., the optimized starting pressure value) those in which the larger number of analyses has an equilibrium tolerance of 30 °C (Fig. 10a). This latter value is the error related to the methodology (Vidal et al., 2006). Wide *T* ranges were obtained for all the samples, but all of them show well defined peaks which are included between 175 and 280 °C in the samples of WU and Dehendar

Table 2
Representative electron microprobe analyses of phengites from the Durkan Complex. Calculation of atoms per formula unit (a.p.f.u.) is based on 11 oxygen.

Locality - Unit	Chah Shahi – western unit						Chah Shahi – eastern unit								
Sample	MK844			MK858			MK820			MK821			MK823		
Mineral	*2*	*3*	*7*	*1*	*3*	*4*	*2*	*5*	*7*	*2*	*4*	*6*	*4*	*5*	*7*
wt.%															
SiO_2	47.26	46.27	49.79	53.28	53.76	54.47	51.16	50.88	51.48	51.69	52.88	52.02	52.18	52.53	53.44
TiO_2	0.43	0.14	0.10	0.17	0.11	0.22	0.19	0.21	0.08	0.36	0.35	0.20	0.04	0.06	0.03
Al_2O_3	28.31	28.36	29.30	21.93	22.62	22.68	25.13	23.91	24.93	26.60	26.72	27.5	21.94	22.07	22.11
FeO	3.82	4.43	3.16	4.98	3.97	4.82	5.28	5.64	4.92	3.38	2.98	2.04	6.92	7.49	6.09
MnO	b.d.l.	0.02	0.01	0.01	0.01	0.03	0.01	b.d.l.	b.d.l.	0.05	0.02	b.d.l.	0.07	0.03	0.04
MgO	2.96	3.17	2.01	4.24	4.20	4.27	3.20	3.50	3.27	2.81	3.29	2.96	3.79	3.71	3.90
CaO	0.43	0.33	0.34	0.03	0.04	0.07	b.d.l.	0.01	b.d.l.	b.d.l.	0.08	0.02	0.05	0.07	0.04
Na_2O	0.26	0.34	0.29	0.10	0.12	0.05	0.34	0.16	0.25	0.19	0.33	0.38	0.07	0.04	0.05
K_2O	8.90	9.72	9.66	10.08	10.06	10.35	9.94	10.33	10.01	9.49	9.46	9.56	10.62	10.65	10.97
Total	92.36	92.78	94.66	94.82	94.89	96.96	95.26	94.64	94.97	94.57	96.11	94.68	95.68	96.64	96.68
a.p.f.u.															
Si	3.265	3.217	3.340	3.604	3.609	3.598	3.454	3.476	3.454	3.462	3.475	3.456	3.552	3.547	3.583
Al^{IV}	0.735	0.783	0.660	0.396	0.391	0.402	0.546	0.524	0.546	0.538	0.525	0.544	0.448	0.453	0.416
Al^{VI}	1.571	1.541	1.656	1.352	1.399	1.364	1.454	1.401	1.454	1.561	1.545	1.610	1.312	1.304	1.331
Ti	0.022	0.007	0.005	0.009	0.006	0.011	0.010	0.011	0.010	0.018	0.017	0.010	0.002	0.003	0.002
Fe^{2+}	0.221	0.258	0.177	0.282	0.223	0.266	0.298	0.322	0.298	0.189	0.164	0.113	0.394	0.423	0.341
Mn	0.000	0.001	0.001	0.001	0.001	0.002	0.001	0.000	0.000	0.003	0.001	0.000	0.004	0.002	0.002
Mg	0.305	0.329	0.201	0.428	0.420	0.421	0.322	0.356	0.322	0.281	0.322	0.293	0.385	0.374	0.390
Ca	0.032	0.025	0.024	0.002	0.003	0.005	0.000	0.001	0.000	0.000	0.005	0.001	0.004	0.005	0.003
Na	0.034	0.046	0.038	0.013	0.016	0.006	0.045	0.021	0.045	0.025	0.042	0.049	0.009	0.005	0.007
K	0.784	0.862	0.827	0.870	0.862	0.872	0.856	0.900	0.856	0.811	0.793	0.810	0.922	0.918	0.938
Total	6.969	7.068	6.929	6.955	6.929	6.947	6.986	7.012	7.013	6.888	6.890	6.887	7.032	7.033	7.015

Note: b.d.l. – below detection limits.

area and between 150 and 350 °C in EU of the Chah Shahi area, respectively (Fig. 10a). These results were compared with those calculated with the Cathelineau and Nieva (1985) geothermometers (Fig. 9a) applied to all the samples, getting a good fit largely included in the error of the method (i.e., ±30 °C).

The phengite-quartz-water method (Dubacq et al., 2010) was applied to samples from the eastern and western units by fixing *T* and $\%Fe^{3+}$ on the base of the results from the chlorite-quartz-water method. For each analysis, the phengite-quartz-water method was applied fixing different *P* value. The results obtained are temperatures that vary with the water content (X_{H2O}). To estimate the metamorphic conditions of the rocks we therefore chose the *T* values based on the concordance of the water content of the phengites analysed, thus obtaining a range of *T* dependent on *P*. We note that, in the ranges of 0.7–1.2 GPa for the western unit and of 0.4–1.3 GPa for the eastern unit, water content (X_{H2O}) > 80 % is reached by each single phengite in a narrow range of temperature (Fig. 10b, e.g. Di Rosa et al., 2020b; Frassi et al., 2022). These temperatures are included within the error of those obtained with the Chlorite-quartz-water method and the Cathelineau and Nieva (1985) geothermometer. Considering the distribution of the single analysis within the *P-T* spaces, a range of 0.6–1.2 GPa and 0.4–1.3 GPa will be used for the tectonic units WU_1 and EU_2 of Chah Shahi area, respectively (Fig. 10b).

Finally, the chlorite-phengite-quartz-water method (Vidal and Parra, 2000) was applied on the chlorite-phengite couples found into the S_1 foliation. Only the cases in which the sum of the energies of independent reactions is lower than 1 kJ were considered. A second selection based on the *T* range previously calculated with the chlorite-quartz-water method combined with the values obtained with the Cathelineau and Nieva (1985) geothermometer has been adopted. We thus propose *P-T* conditions of 0.7–1.0 (±0.2) GPa and 220–280 (±20) °C for the tectonic unit WU_1 and 0.6–1.2 (±0.2) GPa and 160–310 (±20) °C for the tectonic unit EU_2 (Fig. 10c).

5. Discussion

5.1. Significance of the structural evolution of the Durkan Complex within the Makran

Modern and ancient subduction complexes are characterized by various deformation stages occurring at different depths and times of their accretion-subduction history and subsequent exhumation (Platt et al., 1985; Clift and Vannucchi, 2004; Marroni et al., 2004; Ueda, 2005; Meneghini et al., 2009; Kusky et al., 2013). Accordingly, multiscale structural data from the Durkan Complex allow us to recognize a polyphase deformation history achieved in the Makran Accretionary Prism. The Late Cretaceous age of the Durkan Complex (Barbero et al., 2021a), the crosscutting relationships between the observed tectonic features (section 3.2), and the stratigraphic unconformity documented in the Dehendar area (section 3.1) provide constraints for the relative chronology of this deformation history. D_1 and D_2 phases occurred from the latest Late Cretaceous to the early Paleocene, whereas the D_3 phase can be referred to post Eocene times, as indicated by the involvement of the upper Paleocene - Eocene succession along the D_3 thrusts (Fig. 11a). The tectonic significance of these phases will be described hereafter and summarized in Fig. 11.

5.1.1. Latest Late Cretaceous – Early Paleocene stages: Accretion and exhumation in a subduction complex

D_1 developed during the accretion of seamount fragments within the Makran prism (Fig. 11a, b). The occurrence of isoclinal folds associated with a pervasive and continuous axial plane foliation showing metamorphic recrystallization indicates that D_1 occurred at relatively deep levels of the accretionary wedge (Fig. 11b). According to the mineralogical assemblages of the axial plane foliation S_1 and the petrological geothermobarometer, D_1 took place at T = 160–300 °C and P = 0.6–1.2 GPa (Fig. 10c, 11b, 12). Though at the estimated *P-T* conditions lawsonite should be stable, the lack of this mineral in the stud-

UNCORRECTED PROOF

Table 3
Representative electron microprobe analyses of amphibole from the Durkan Complex. Calculation of atoms per formula unit (a.p.f.u.) is based on 23 oxygen.

Locality - Unit	Chah Shahi – eastern unit			Dehendar		
Sample	MK823			MK507		
Mineral	*Amp5*	*Amp8*	*Amp10*	*Amp4*	*Amp8*	*Amp9*
wt.%						
SiO_2	55.13	55.39	55.81	55.36	54.63	53.59
TiO_2	0.04	0.07	0.02	0.06	0.08	0.03
Al_2O_3	0.84	1.31	0.83	2.23	1.19	2.14
FeO	14.57	14.58	14.65	23.05	19.21	16.53
MnO	0.30	0.30	0.24	0.17	0.30	0.36
MgO	14.19	14.02	14.90	8.45	12.16	13.36
CaO	11.94	10.72	10.84	1.87	8.31	11.01
Na_2O	0.69	1.24	1.31	6.51	2.47	1.12
K_2O	0.08	0.05	0.09	0.04	0.06	0.09
Total	100.53	99.90	101.10	100.94	101.27	100.73
a.p.f.u.						
Si	7.941	7.971	7.931	7.992	7.844	7.725
Al^{IV}	0.059	0.029	0.069	0.008	0.156	0.275
Al^{VI}	0.084	0.194	0.071	0.371	0.045	0.089
Ti	0.005	0.007	0.002	0.006	0.009	0.003
Fe^{3+}	0.072	0.161	0.316	1.215	0.839	0.449
Fe^{2+}	1.755	1.594	1.425	1.568	1.468	1.544
Mn	0.036	0.036	0.029	0.021	0.037	0.044
Mg	3.047	3.008	3.157	1.819	2.603	2.871
Ca	1.843	1.653	1.651	0.289	1.278	1.700
Na	0.193	0.345	0.361	1.822	0.688	0.314
K	0.015	0.009	0.016	0.008	0.010	0.016
Total	15.050	15.007	15.028	15.119	14.977	15.030
X_{Mg}	0.63	0.65	0.69	0.54	0.64	0.65

Note: $X_{Mg} = Mg / (Mg + Fe^{2+})$; b.d.l. – below detection limits.

ied samples do not contrast our geothermobarometric estimates. In fact, lawsonite stability is controlled by several other factors such as the bulk rock composition of the protoliths as well as the composition and amount of water during the metamorphism (Poli and Schmidt, 2002; Manzotti et al., 2021). In addition, during both prograde and peak metamorphism lawsonite could have been replaced by chlorite, muscovite, and epidote aggregates as similarly suggested in literature (e.g., Manzotti et al., 2021). The *P-T* estimates for D_1 correspond to a depth of 25–40 km and are coherent with deformation at blueschist facies conditions within the Makran subduction complex during the latest Late Cretaceous – early Paleocene ages (Fig. 11b and 12). These *P-T* conditions are typical of high *P* – low *T* metamorphism of cold subduction zones characterized by geothermal gradients in the range 7–8 °C/km (Fig. 12a). Similar thermal conditions have been proposed for the Siah Kuh subducted seamount in the neighbouring Zagros suture zone (Fig. 12a; Bonnet et al., 2020). *P-T* estimates on the Bajgan Complex in the western North Makran (Pandolfi et al., 2021; Barbero et al., 2022), the blueschist units in the eastern North Makran (Hunziker et al., 2017; Omrani et al., 2017), and the Ashin and Seghin complexes in the Zagros suture zone (e.g., Angiboust et al., 2016) suggest warmer thermal gradient during the subduction of the NeoTethys (Fig. 12a). Angiboust et al. (2016) hypothesized the cooling of the thermal gradient of the NeoTethyan subduction zones between 95 Ma and 65 Ma, proposing that this cooling may have been related either to acceleration of closure across the NeoTethys or to the subduction of oceanic lithosphere with a cool thermal regime. Similarly, data from the Durkan Complex and their comparison with others metamorphic units in the western and eastern North Makran suggest that the thermal gradient in the Makran subduction zones could have significantly changed both along strike and over time. The D_1 folding was also coupled with the development of W-verging D_1 shear zones along the overturned limb of macro-scale anticlines (Figs. 2 and 3). The occurrence of these shear zones indicates that the observed juxtaposition of tectonic slices from different seamount settings occurred during the D_1 phase. The nature of these shear zones with a foliated matrix showing shear bands and S—C structures, and their occurrence along D_1 folds limb suggest deformation in a brittle-ductile regime indicating that the accretion of the fragments of different seamount successions occurred with alternating diffuse (i.e., folding) and localized (i.e., shear zone) deformations. D_1 deformation style is compatible with underplating of seamount materials and can be interpreted as related to non-coaxial deformation along and/or above the basal décollement of the North Makran prism (Fig. 11b), as seen in several world-wide fossil accretionary prisms (e.g., Isozaki et al., 1990; Kimura and Mukai, 1991; Isozaki, 1997; Kusky and Bradley, 1999; Marroni et al., 2004; Ueda, 2005; Vannucchi et al., 2006; Meneghini et al., 2009; Wakabayashi, 2017; Agard et al., 2018; Tewksbury-Christle et al., 2021).

D_2 is characterized by folds deforming D_1 structural elements with sub-horizontal axial plane associated with an axial plane foliation, which is selectively development according to the types and rheology of the rocks, ranging from a disjunctive cleavage in arenitic and limestone beds to a crenulation cleavage in the shale. The characteristic of the S_2 foliation (i.e., disjunctive and crenulation cleavage without metamorphic recrystallization) suggest that D_2 phase developed at shallower structural levels with respect to D_1 blueschist phase. These evidence and the overprinting relationships between D_1 and D_2 structures clearly suggest that D_2 phase developed after the D_1 underplating stage, most likely during the progressive exhumation of the accreted units (Fig. 11a, c). In addition, the association of folds with sub-horizontal axial planes and low-angle extensional faults striking parallel to the fold axis well agrees with an exhumation phase during which the maximum principal stress axis was subvertical (Fig. 11c). This agrees with data from many fossil accretionary prisms worldwide, where the combination of sub-horizontal folds and normal faults acts in equilibrating the critical taper angle during the exhumation of the previously accreted units and after the thickening caused by the continuous underplating (e.g., Davis et al., 1983; Platt, 1986, 1993; Marroni et al., 2004; Ueda, 2005; Meneghini et al., 2020). D_2 exhumation can also have been favoured by subduction of relatively high seamounts that could have promoted uplift and extension of the prism close to the incoming seamount and the exhumation of the underplated units (Fig. 11c). This interpretation agrees with observations from both modern and fossil convergent margins (e.g., Lallemand and Le Pichon, 1987; Park et al., 1999; Ueda, 2005) and from numerical modelling (Dominguez et al., 1998; Ruh et al., 2016; Ruh, 2020). In this context, the uplift can be followed by extension and subsidence of the fore-arc and the inner wedge while the subducted seamount progressively moves down along the subduction zone (Park et al., 1999). Extensional deformation during seamount subduction is also described by numerical modelling seaward of and above the subducting seamount (Ruh et al., 2016; Ruh, 2016; Wang et al., 2021).

5.1.2. Post-Eocene stage: Post accretion sedimentation and out-of-sequence thrusting

The unconformable deposition of the upper Paleocene – Eocene turbiditic siliciclastic succession onto the exhumed Durkan Complex marked the transition from D_2 and D_3 phases (Fig. 11a, d). This succession is characterized by alternating quartz-rich arenites absent in the Durkan succession and suggests the erosion of continental basement rocks and/or volcanic and intrusive acidic rocks. During this stage, a new accretionary frontal wedge existed, and it is now represented by the Coloured Mélange (Fig. 11d). This includes remnants of the subducting oceanic lithosphere, Cretaceous pelagic sedimentary cover, and Paleocene siliciclastic turbiditic successions and it is thought to have formed by offscraping in the trench of a north dipping subduction zone

CORRECTED PROOF

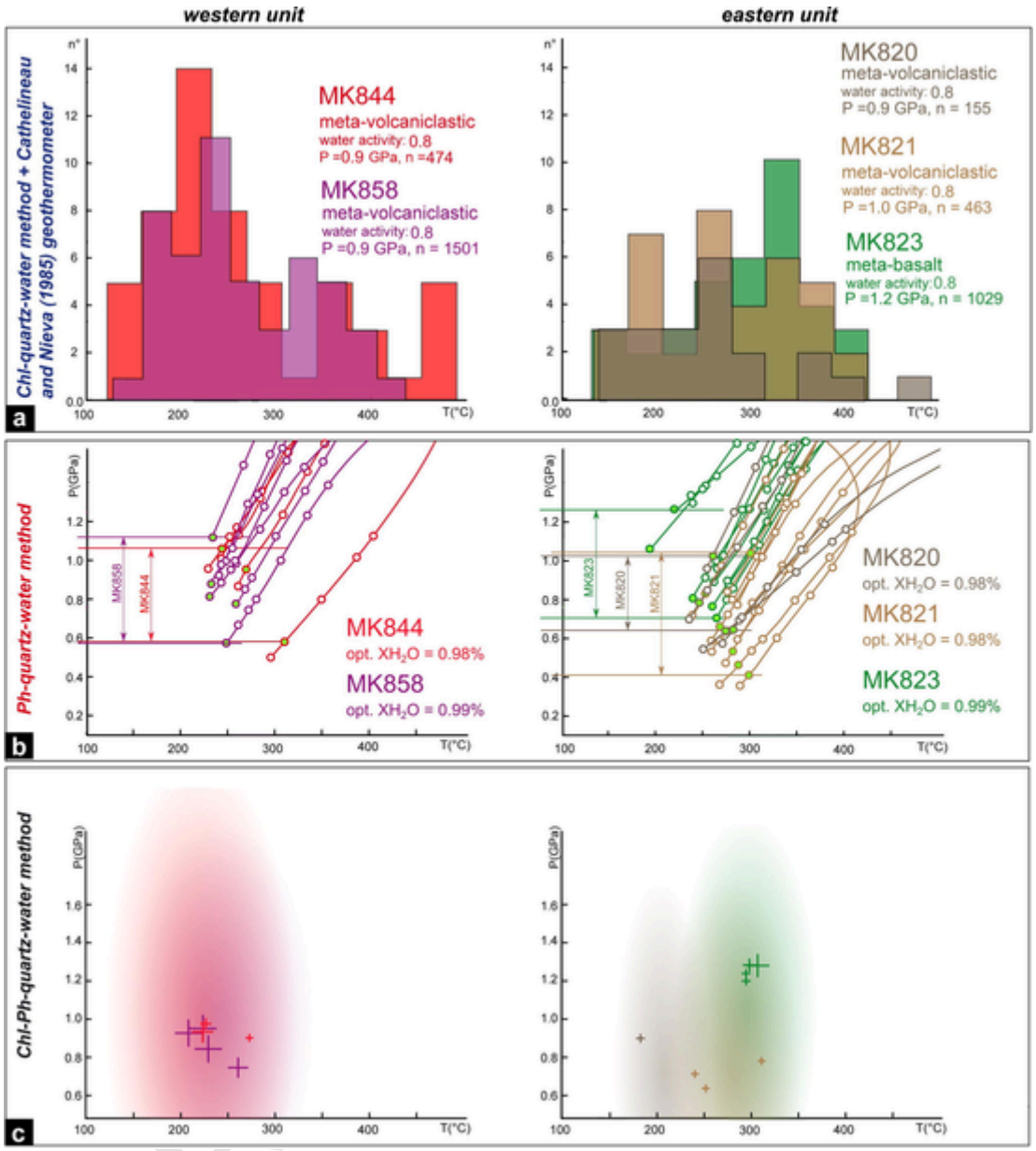

Fig. 10. Results of the pressure–temperature (*P-T*) estimates for the western unit 2 (left side) and eastern unit 1 (right side) in the Chah Shahi area (for locations of samples see Fig. 2a, 2b). The same colour is used for the same sample in the legend (i.e., name and indications within the diagrams), histogram and box. (a) Histogram showing the *T* results obtained with the chlorite-quartz-water method; (b) results of the phengite-quartz-water method. Open circles along each line indicate different water contents (from X_{H2O} = 0.99 to X_{H2O} = 0.95) for single phengite analysis; the position in the *P-T* diagram in which the optimized value of X_{H2O} for each sample is reached is indicated by solid circles. The *P* range (horizontal lines) for each sample is assumed considering the *P* values at which each single phengite analysis (i.e., lines) reached the optimized X_{H2O}; (c) *P-T* conditions estimated with the chlorite-phengite-quartz-water method. The results (all the equilibrium reached with chlorite-phengite couples for which the sum of energy required do not exceed 1000 J) are plotted as crosses. The size of crosses is proportional to the energy involved in the reaction. Coloured areas in the background indicate the *T* ranges obtained in panel (a).

during the Paleocene (McCall and Kidd, 1982; McCall, 2002; Burg, 2018; Saccani et al., 2018; Esmaeili et al., 2020, Esmaeili et al., 2022). The Durkan Complex represented the indenter of this actively building frontal wedge (Fig. 11d). This interpretation agrees with the provenance data from the turbidites from the Coloured Mélange, which consist of litharenites and feldspathic litharenites fed by the erosion of an unroofed volcanic arc (Esmaeili et al., 2020). This hypothesis also agrees with the provenance data from the turbidites of the Inner and Outer Makran domains that point out for a magmatic arc and recycled accreted sediments as the main source rocks (Mohammadi et al., 2016, 2017; Burg, 2018).

D_3 involved both the Durkan Complex and the upper Paleocene – Eocene succession and it is characterized by a thrusting deformation associated with folding close to the main thrust zones (section 3.2.3). These features suggest a post-Eocene compressive deformation of the inner part (i.e., the present-day North Makran domain) of the Makran subduction complex (Fig. 11d). The significance and age of this phase is still puzzling as more biostratigraphic and structural data are needed from the upper Paleocene – Eocene and post-Eocene stratigraphic successions. Published structural and stratigraphic data from the Inner, Outer, and Coastal Makran indicate that these domains have been deformed from the early-middle Miocene to the Pliocene during the propagation of a S-verging fold-and-thrust system (Dolati, 2010; Burg et al.,

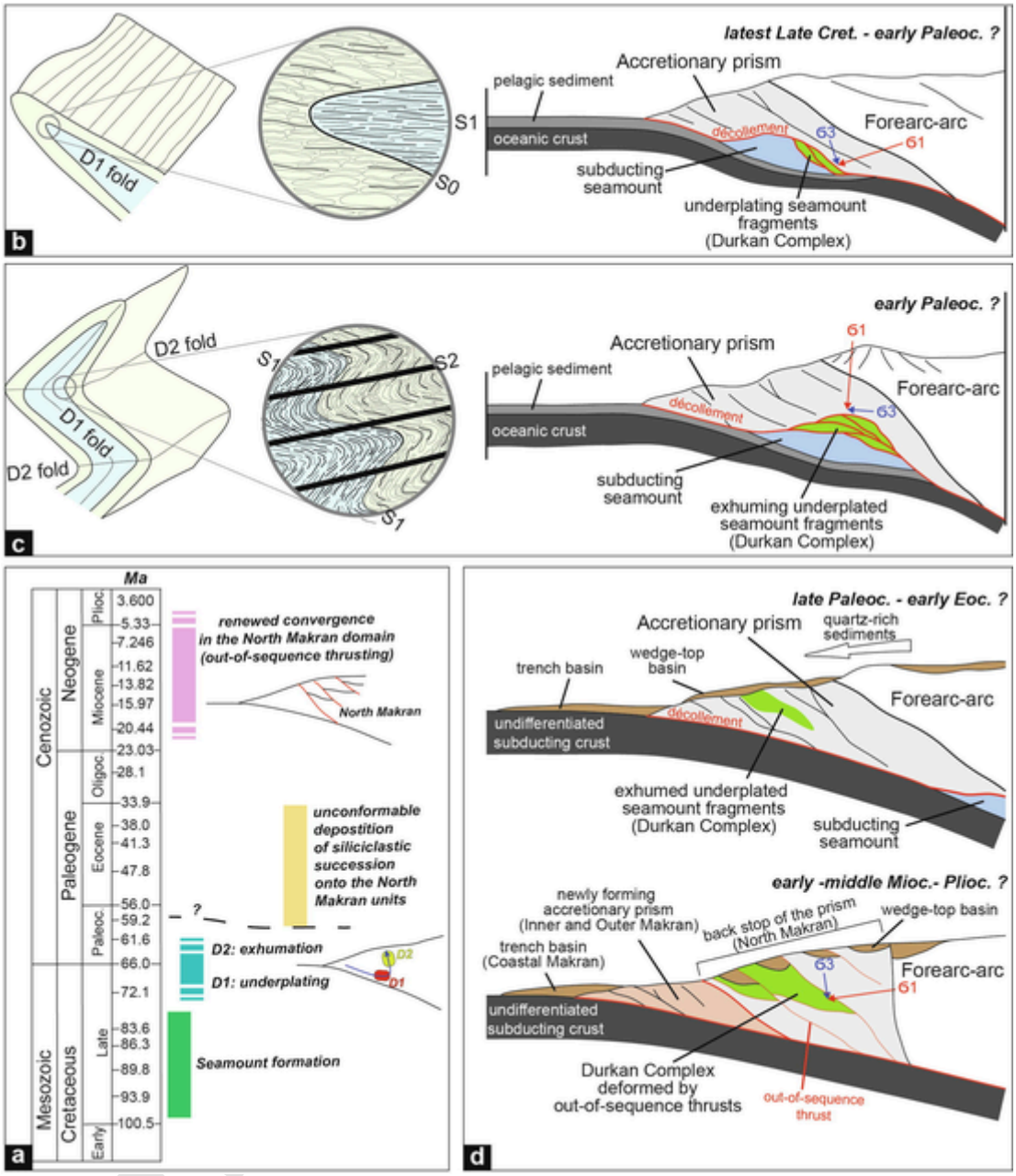

Fig. 11. (a) Summary of the Late Cretaceous to middle Miocene-Pliocene tectonic evolution of the Makran Accretionary Prism. Cartoons showing conceptual models for the tectonic evolution and deformative mechanism for D_1 (b), D_2 (c), and D_3 (d) phases. Orientation of stress axes σ_1 and σ_3 during seamount subduction are based on Ruh et al. (2016) and Wang et al. (2021).

2013). Distributed shortening was assumed to be an important mechanism of deformation by Burg et al. (2013), though the decrease of apatite-zircon fission-track ages and the progressive deactivation of thrusts from north to south indicate an oceanward propagation of the deformation during this time (Dolati, 2010; Burg et al., 2013). D_3 deformation phase recognized in this study can thus be correlated with the early-middle Miocene - Pliocene compressional stage that affected the Makran subduction complex at regional-scale, or alternatively as a slightly older (i.e., Oligocene – Miocene) phase. In both cases, D_3 thrusts likely represent out-of-sequence thrusts that reworked the nappe pile formed during the D_1 and D_2 phases (Fig. 11d). These thrusts are interpreted as linked to the Bashakerd Thrust, which corresponds to a first order tectonic element juxtaposing the North Makran domain to the Inner Makran (Dolati, 2010; Burg et al., 2013), and they are responsible for the final structuration of the units of the North Makran domain (Fig. 11d).

5.2. Incorporation of seamount fragments within an accretionary prism: The role of seamount stratigraphy

Our structural data indicate that fragments of the Durkan seamounts chain (Fig. 13a; Barbero et al., 2021a, b) have been underplated within the Makran subduction complex during D_1 deformation phase at blueschist facies condition (Fig. 12). The underplating produced several tectonic slices juxtaposed by D_1 shear zones (Fig. 11a). The evidence that D_1 shear zones show a block-in-matrix fabric with lens-shaped marbles and *meta*-basalts blocks within a foliated volcaniclastic matrix (Fig. 4f, g), suggest that deformation concentrated and propagated along a specific rheological and stratigraphic horizon. This shear surface devel-

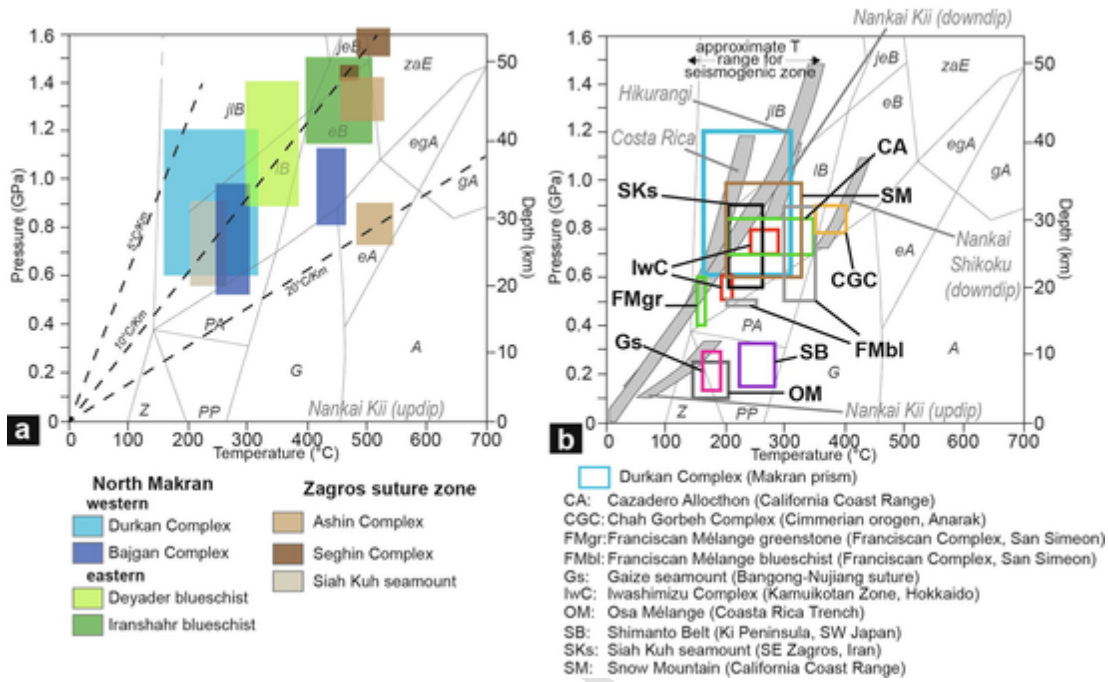

Fig. 12. (a) Pressure–temperature (*P-T*) range for the Durkan Complex and other metamorphic units in the North Makran domain (data from Hunziker et al., 2017; Omrani et al., 2017; Pandolfi et al., 2021), and the south-eastern Zagros suture zone (data source Angiboust et al., 2016; Bonnet et al., 2020). Black dotted lines indicate geothermal gradients. (b) Comparison of the *P-T* range of the Durkan seamount and selected subducted seamounts from worldwide accretionary and collisional belts. Data source: CA, Maruyama and Liou, 1989; CGC: Buchs et al., 2013; IwC: Ueda, 2005; Gs, Zeng et al., 2021; OM: Vannucchi et al., 2006; SKs: Bonnet et al., 2020; SB: Hashimoto et al., 2002; SM: MacPherson, 1983; FMgr and FMbl: Ukar and Cloos, 2014, 2015. The approximate *P-T* range at the source of slow earthquakes from modern convergent margin showing seamount subduction (grey fields, data source from Kirkpatrick et al., 2021 and references therein) and *T* range for the seismogenic zone along subduction complexes (Hyndman et al., 1997) are also shown. Metamorphic facies abbreviations: A, amphibolite; eA, epidote amphibolite; eB, epidote blueschist; egA, epidote-garnet amphibolite; G, greenschist; gA, garnet amphibolite; jeB, jadeite-epidote blueschist; jlB, jadeite-lawsonite blueschist; lB, lawsonite blueschist; PA, prehnite-actinolite; PP, prehnite-pumpellyite; Z, zeolite; zaE, zoisite-amphibole-eclogite facies.

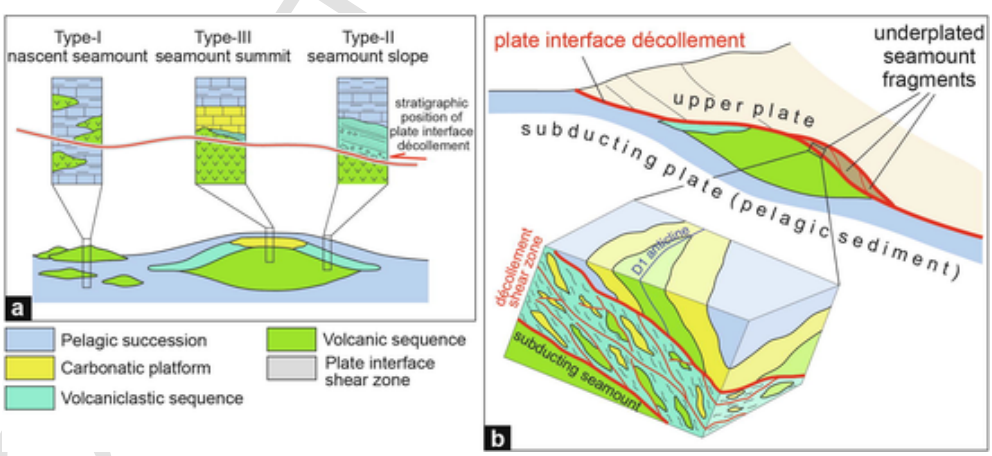

Fig. 13. (a) Conceptual model for the localization of the plate interface décollement during subduction of seamounts; (b) décollement shear zone structural architecture during underplating of seamount fragments. Figures are loosely based on Barnes et al. (2020). Stratigraphic columns in (a) are from Barbero et al. (2021a).

oped at the boundary between the volcanic and volcano-sedimentary sequence of the seamount slope succession, which is rich of volcaniclastic sediments (Fig. 13a). The internal arrangement of the D_1 shear zones with a clear block-in-matrix fabric and their pluridecametric thickness (Fig. 4g and Fig. 13b for conceptual model) are well comparable with broken-formations formed by the tectonic disruption along the basal décollement of a heterogeneous Ocean Plate Stratigraphy without including exotic blocks (e.g., Wakita, 2015; Wakabayashi, 2017; Festa et al., 2018, Festa et al., 2019, Festa et al., 2022 and reference therein). All these evidence document that (i) D_1 shear zones can be interpreted as the basal décollement of the prism and (ii) seamount slope succession has a key role in controlling shear zones localization and propagation, as suggested for subducting (e.g., Barnes et al., 2020) and subducted seamounts (e.g., Vannucchi et al., 2006; Clarke et al., 2018; Bonnet et al., 2020). Once the D_1 décollement propagated within the seamount slope sediments, it is likely able to further step down within the superficial part of the volcanic edifice of the seamount, as it is composed of hydrothermally altered basalts covered by carbonate platform limestone (Fig. 13a, b). The altered basalts likely behave as a weak horizon, as described by Kimura and Ludden, (1995), who suggest that altered basaltic oceanic crust may represent a preferential horizon for the localization of the décollement. The propagation of the décollement inside

the seamount volcanic edifice is testified by the incorporation of basalts and carbonate platform blocks within the block-in-matrix D_1 shear zones (Fig. 4f, 13b for conceptual model). This mechanism triggered the underplating of tectonic slices composed of the upper part of the seamount with rather thin volcanic sequence at the base of most of the accreted units (Figs. 2, 3 and Fig. 13b for conceptual model).

The comparison of the proposed model with previous works on active and fossils subduction complexes bearing seamounts in the subducting plate strongly support our conclusion (e.g., Cloos and Shreve, 1996; Vannucchi et al., 2006; Clarke et al., 2018; Barnes et al., 2020; Bonnet et al., 2020; Zeng et al., 2021). Generally, seamounts entering within a convergent margin are largely subducted and just their superficial parts can be accreted into the accretionary prism (Cloos and Shreve, 1988, 1996; Isozaki et al., 1990; Isozaki, 1997; Park et al., 1999; Ueda, 2005; Yang et al., 2015; Bonnet et al., 2019, Bonnet et al., 2020), as schematically shown in Fig. 13b. Only exceptionally high and large seamounts and oceanic plateau can entirely be accreted to the subduction zone, jamming the subduction zone and inducing collision-like deformation (Cloos, 1993; Kerr et al., 1998). Although fragments of seamounts are thought to be incorporated within the accretionary prism with different models and at different depths or structural levels (Isozaki et al., 1990; Cloos and Shreve, 1996; Isozaki, 1997; Ueda, 2005; Vannucchi et al., 2006; Yang et al., 2015; Clarke et al., 2018; Zeng et al., 2021), our interpretation well agrees with what recently proposed by Bonnet et al. (2019, Bonnet et al., 2020), who suggested that the heterogeneities of the seamount stratigraphic architecture plus the role of serpentinites from the subducting plate likely play a major role in controlling the localization of the deformation. Accordingly, other authors indicate that a significant role for the seamount fragments accretion is played by the seamount slope successions (e.g., Vannucchi et al., 2006; Clarke et al., 2018; Barnes et al., 2020), supporting our observation and conclusion.

Finally, studies on active convergent margins outline that seamount subduction can significantly influence the seismic activity at subduction zone, both promoting (e.g., Cloos, 1992; Scholz and Small, 1997; Bilek et al., 2003) or restraining (e.g., Kodaira et al., 2000; Das and Watts, 2009; Wang and Bilek, 2011; Geersen et al., 2015) large earthquakes ruptures and their propagations. Structural investigations on accreted seamounts in ancient subduction complexes have the potential to provide data complementary to the geophysical and seismological dataset from modern subduction zones. In fact, fragments of seamounts are found in several mountain belts such as the Japanese Islands (Isozaki et al., 1990; Hashimoto et al., 2002; Ueda, 2005), the Cimmerian orogenic belt (Bagheri and Stampfli, 2008; Buchs et al., 2013), the Costa Rica exhumed accretionary prism (Vannucchi et al., 2006), the Zagros Belt (Bonnet et al., 2019, Bonnet et al., 2020), the Asian collisional belts (Yang et al., 2015, 2022; Safonova et al., 2016; Wan et al., 2021; Zeng et al., 2021), the California Coastal Range and the Franciscan Complex (MacPherson, 1983; Maruyama and Liou, 1989; Ukar and Cloos, 2014, 2015). Tough differing in age and location, it is important to note that these seamount fragments, including the accreted Durkan seamounts chain, are deformed within a subduction complex at *T-P* condition that are in the range of those typical of seismogenic zone and slow earthquakes in modern convergent margins (Fig. 12b). Therefore, these data suggest that field-based studies on accreted seamount in ancient subduction complexes have the potential to shed light on the mechanism of deformation and role of subducting seamount during seismic cycle.

6. Conclusion

The western Durkan Complex is a tectonic element of the North Makran domain, which has recently been interpreted as remnants of a Late Cretaceous seamount chain. Our macro- to micro-scale structural study documents its tectono-metamorphic evolution. The main conclusions of this study are summarized as follows.(1) The Durkan Complex is composed by several tectonic units bounded by NW- to NNW-striking and SW- to W-verging thrust systems. The stratigraphic successions in the different slices mainly represent the slope and summit of Late Cretaceous seamounts. These successions are both tectonically juxtaposed and unconformably covered by an upper Paleocene – Eocene stratigraphic succession. (2) The crosscutting relationships between the structural elements and the stratigraphic uniformities allow us to recognize three phases of deformations, namely D_1, D_2, and D_3. D_1 is characterized by W-verging folds, locally associated with shear zones along the limbs, which show block-in-matrix fabric and are mainly composed of volcaniclastic material from the seamount slope successions. D_2 is characterized by NE- to E-verging open to close folds. D_1 and D_2 folds are unconformably covered by the upper Paleocene – Eocene succession. D_3 is characterized by W-verging thrust zones during the Miocene – Pliocene stages.(3) The microstructural study indicate that the S_1 foliation shows different features and dynamic recrystallization based on the rock type. Relict magmatic textures are generally preserved in the *meta*-basalts. The foliation in the *meta*-volcaniclastic rocks and the *meta*-sedimentary rocks is defined by chlorite, white mica, clay minerals, calcite, quartz-albite aggregate in different proportions according to the rock types.(4) Petrological geothermobarometers on the S_1 paragenesis suggest that D_1 developed during blueschists facies metamorphism, with *P* in the range 0.6 – 1.2 GPa and *T* in the range 160–300 °C.

These data allow to reconstruct the Late Cretaceous – Miocene-Pliocene structural evolution of the western Durkan Complex within the Makran prism. D_1 and D_2 phases likely record the Late Cretaceous – early Paleocene underplating of seamount fragments at blueschist facies conditions, and the subsequent exhumation at shallower structural levels of the prism, respectively. These stages are followed by a renewed phase of convergence showing the activation of out-of-sequence thrusts, likely during the Miocene – Pliocene. As a rule, we suggest that the stratigraphy of the subducting seamount possibly controls the position of the basal décollement of the prism during underplating. In detail, the occurrence of thick volcaniclastic succession around the subducting seamount likely plays a key role for the localization and propagation of the décollement within the upper part of the seamount edifice. Our results provide new data for a better understanding of the deformation pattern of the accretionary prism during the subduction of topographic relief.

Declaration of Competing Interest

The authors declare that they have no known competing financial interests or personal relationships that could have appeared to influence the work reported in this paper.

Acknowledgements

The research has been funded by Darius Project (Head M. Marroni), PRA project of the Pisa University (Head S. Rocchi), IGG-CNR, FAR-2018 Project of the Ferrara University (Head E. Saccani). We sincerely thank Mr. Ahmad Behboodi for his fundamental assistance in organizing field work, and PhD student Ahmad Nateghpour from Kharazmi University for his help during field work. The authors are grateful to the University Centrum for Applied Geosciences (UCAG) for the access to the E. F. Stumpfl electron microprobe laboratory. We would also like to express our gratitude to G. Bonnet for his thorough comments to an earlier version of this manuscript, which encouraged us to greatly improve this article. G. Bonnet and G. Yang are kindly acknowledged for their thorough reviews from which we have greatly benefited in revising our paper. I. Safonova is kindly acknowledged for the careful editorial handling.

CORRECTED PROOF

Appendix A. Supplementary data

Supplementary data to this article can be found online at https://doi.org/10.1016/j.gsf.2022.101522.

References

Agard, P., Plunder, A., Angiboust, S., Bonnet, G., Ruh, J., 2018. The subduction plate interface: rock record and mechanical coupling (from long to short timescales). Lithos 320–321, 537–566. https://doi.org/10.1016/j.lithos.2018.09.029.

Angiboust, S., Agard, P., Glodny, J., Omrani, J., Oncken, O., 2016. Zagros blueschists: Episodic underplating and long-lived cooling of a subduction zone. Earth Planet. Sci. Lett. 443, 48–58. https://doi.org/10.1016/j.epsl.2016.03.017.

Bagheri, S., Stampfli, G.M., 2008. The Anarak, Jandaq and Posht-e-Badam metamorphic complexes in central Iran: New geological data, relationships and tectonic implications. Tectonophysics 451 (1–4), 123–155. https://doi.org/10.1016/j.tecto.2007.11.047.

Bangs, N.L.B., Gulick, S.P.S., Shipley, T.H., 2006. Seamount subduction erosion in the Nankai Trough and its potential impact on the seismogenic zone. Geology 34 (8), 701–704. https://doi.org/10.1130/G22451.1.

Barbero, E., Delavari, M., Dolati, A., Vahedi, L., Langone, A., Marroni, M., Pandolfi, L., Zaccarini, F., Saccani, E., 2020. Early Cretaceous plume–ridge interaction recorded in the Band-e-Zeyarat Ophiolite (North Makran, Iran): New constraints from petrological, mineral chemistry, and geochronological data. Minerals 10 (12), 1100. https://doi.org/10.3390/min10121100.

Barbero, E., Delavari, M., Dolati, A., Saccani, E., Marroni, M., Catanzariti, R., Pandolfi, L., 2020. The Ganj Complex reinterpreted as a Late cretaceous volcanic arc: Implications for the geodynamic evolution of the North Makran domain (Southeast Iran). J. Asian Earth Sci. J. Asian Earth Sci. 195, 104306. doi:10.1016/j.jseaes.2020.104306

Barbero, E., Delavari, M., Dolati, A., Langone, A., Pandolfi, L., Marroni, M., Saccani, E., 2022. New geochemical and age data on the Bajgan Complex (Makran Accretionary Prism, SE Iran): Implications for the redefinition of its tectonic setting of formation from a Paleozoic continental basement to a Cretaceous oceanic domain. Mediterranean Geosciences Union Annual Meeting (MedGU-21), Istanbul, November 25-28, 2021, Advances in Science, Technology & Innovation, in press, 4 pp. SpringerLink Digital Library, 4 p.

Barbero, E., Pandolfi, L., Delavari, M., Dolati, A., Saccani, E., Catanzariti, R., Luciani, V., Chiari, M., Marroni, M., 2021a. The western Durkan Complex (Makran Accretionary Prism, SE Iran): A Late Cretaceous tectonically disrupted seamounts chain and its role in controlling deformation style. Geosci. Front. 12, 101106. https://doi.org/10.1016/j.gsf.2020.12.001.

Barbero, E., Zaccarini, F., Delavari, M., Dolati, A., Saccani, E., Marroni, M., Pandolfi, L., 2021b. New evidence for Late Cretaceous plume-related seamounts in the Middle East sector of the Neo-Tethys: Constraints from geochemistry, petrology, and mineral chemistry of the magmatic rocks from the western Durkan Complex (Makran Accretionary Prism, SE Iran. Lithos 396–397, 106228. https://doi.org/10.1016/j.lithos.2021.106228.

Barnes, P.M., Wallace, L.M., Saffer, D.M., Bell, R.E., Underwood, M.B., Fagereng, A., Meneghini, F., Savage, H.M., Rabinowitz, H.S., Morgan, J.K., Kitajima, H., Kutterolf, S., Hashimoto, Y., Engelmann de Oliveira, C.H., Noda, A., Crundwell, M.P., Shepherd, C.L., Woodhouse, A.D., Harris, R.N., et al., 2020. Slow slip source characterized by lithological and geometric heterogeneity. Sci. Adv. 6(13), eaay3314. doi:10.1126/sciadv.aay3314.

Barrier, E., Vrielynck, B., Brouillet, J.F., Brunet, M.F., 2018. Paleotectonic reconstruction of the central Tethyan realm. Tectono-sedimentary-palinspastic maps from Late Permian to Pliocene. Atlas of 20 maps (scale: 1:15,000,000). CCGM/CGMW, Paris, http://www.ccgm.org.

Bilek, S.L., Schwartz, S.Y., DeShon, H.R., 2003. Control of seafloor roughness on earthquake rupture behavior. Geology 31 (5), 455–458. https://doi.org/10.1130/0091-7613(2003)031<0455:COSROE>2.0.CO;2.

Bonnet, G., Agard, P., Angiboust, S., Fournier, M., Omrani, J., 2019. No large earthquakes in fully exposed subducted seamount. Geology 47 (5), 407–410. https://doi.org/10.1130/G45564.1.

Bonnet, G., Agard, P., Angiboust, S., Monié, P., Fournier, M., Caron, B., Omrani, J., 2020. Structure and metamorphism of a subducted seamount (Zagros suture, Southern Iran). Geosphere 16, 62–81. https://doi.org/10.1130/GES02134.1.

Buchs, D.M., Bagheri, S., Martin, L., Hermann, J., Arculus, R., 2013. Paleozoic to Triassic ocean opening and closure preserved in Central Iran: Constraints from the geochemistry of meta-igneous rocks of the Anarak area. Lithos 172–173, 267–287. https://doi.org/10.1016/j.lithos.2013.02.009.

Burg, J.-P., 2018. Geology of the onshore Makran accretionary wedge: Synthesis and tectonic interpretation. Earth-Sci. Rev. 185, 1210–1231. https://doi.org/10.1016/j.earscirev.2018.09.011.

Burg, J.-P., Bernoulli, D., Smit, J., Dolati, A., Bahroudi, A., 2008. A giant catastrophic mud-and-debris flow in the Miocene Makran. Terr. Nova 20, 188–193. https://doi.org/10.1111/j.1365-3121.2008.00804.x.

Burg, J.-P., Dolati, A., Bernoulli, D., Smit, J., 2013. Structural style of the Makran tertiary accretionary complex in SE Iran. In: Al Hosani, K., Roure, F., Ellison, R., Lokier, S. (Eds.), Lithosphere Dynamics and Sedimentary Basins: The Arabian Plate and Analogues. Frontiers in Earth Sciences. Springer, Heidelberg, pp. 239–259. https://doi.org/10.1007/978-3-642-30609-9_12.

Cathelineau, M., Nieva, D., 1985. A chlorite solid solution geothermometer. The Los Azufres (Mexico) geothermal system. Contrib. Mineral. Petrol. 91, 235–1224.

Clarke, A.P., Vannucchi, P., Morgan, J., 2018. Seamount chain–subduction zone interactions: Implications for accretionary and erosive subduction zone behaviour. Geology 46 (4), 367–370. https://doi.org/10.1130/G40063.1.

Clift, P., Vannucchi, P., 2004. Controls on tectonic accretion versus erosion in subduction zones: Implications for the origin and recycling of the continental crust. Rev. Geophys. 42 (2), RG2001. https://doi.org/10.1029/2003RG000127.

Cloos, M., 1992. Thrust-type subduction-zone earthquakes and seamount asperities: A physical model for seismic rupture. Geology 20 (7), 601–604. https://doi.org/10.1130/0091-7613(1992)020<0601:TTSZEA>2.3.CO;2.

Cloos, M., 1993. Lithospheric buoyancy and collisional orogenesis: Subduction of oceanic plateaus, continental margins, island arcs, spreading ridges, and seamounts. Geol. Soc. Am. Bull. Geol. Soc. Am. Bull. 105 (6), 715–737. https://doi.org/10.1130/0016-7606(1993)105<0715:LBACOS>2.3.CO;2.

Cloos, M., Shreve, R.L., 1996. Shear zone thickness and the seismicity of Chilean- and Mariana-type subduction zones. Geology 24, 107–110. doi:10. 1130/0091- 7613 (1996)024 <0107: SZTATS>2.3.CO;2.

Cloos, M., Shreve, R., 1988. Subduction-channel model of prism accretion, melange formation, sediment subduction, and subduction erosion at convergent plate margins.1. Background and description. Pure Appl. Geophys. 128, 455–500. https://doi.org/10.1007/BF00874548.

Das, S., Watts, A.B., 2009. Effect of subducting seafloor topography on the rupture characteristics of great subduction zone earthquakes. In: Lallemand, S., Funiciello, F. (Eds.), Subduction Zone Geodynamics. Springer, Berlin, Heidelberg, pp. 103–118.

Davis, D., Suppe, J., Dahlen, F.A., 1983. Mechanics of fold-and-thrust belts and accretionary wedges. J. Geophys. Res. J. Geophys. Res. 88 (B2), 1153–1172.

Dercourt, J., Zonenshian, L.P., Ricou, L.E., Kazmin, V.G., LePichon, X., Knipper, A.L., Grandjacquet, C., Sbortshikov, M., Geyssant, J., Lepvrier, C., Pechersky, D.H., Boulin, J., Sibuet, J.C., Savostin, L.A., Sorokhtin, O., Westphal, M., Bazhenov, M.L., Lauer, J.P., Biju-Duval, B., 1986. Geological evolution of the Tethys Belt from the Atlantic to the Pamir since the Lias. Tectonophysics 123, 241–315.

Di Rosa, M., Frassi, C., Marroni, M., Meneghini, F., Pandolfi, L., 2020a. Did the "Autochthonous" European foreland of Corsica Island (France) experience Alpine subduction? Terr. Nova 32 (1), 34–43. https://doi.org/10.1111/ter.12433.

Di Rosa, M., Meneghini, F., Marroni, M., Frassi, C., Pandolfi, L., 2020b. The coupling of high-pressure oceanic and continental units in Alpine Corsica: Evidence for syn-exhumation tectonic erosion at the roof of the plate interface. Lithos 354–355, 105328. https://doi.org/10.1016/j.lithos.2019.105328.

Dolati, A., 2010. Stratigraphy, Structure Geology and Low-temperature Thermochronology Across the Makran Accretionary Wedge in Iran, ETH Zurich, p. 165. PhD thesis.

Dolati, A., Burg, J.-P., 2013. Preliminary fault analysis and paleostress evolution in the Makran Fold-and-Thrust Belt in Iran. In: Al Hosani, K., Roure, F., Ellison, R., Lokier, S. (Eds.), Lithosphere Dynamics and Sedimentary Basins: The Arabian Plate and Analogues. Frontiers in Earth Sciences. Springer, Heidelberg, pp. 261–277. https://doi.org/10.1007/978-3-642-30609-9_13.

Dominguez, S., Lallemand, S.E., Malavieille, J., von Huene, R., 1998. Upper plate deformation associated with seamount subduction. Tectonophysics 293, 207–224. https://doi.org/10.1016/S0040-1951(98)00086-9.

Dubacq, B., Vidal, O., De Andrade, V., 2010. Dehydration of dioctahedral aluminous phyllosilicates: thermodynamic modelling and implications for thermobarometric estimates. Contrib. Mineral. Petrol. 159, 159–174.

Eftekhar-Nezhad, J., Arshadi, S., Mahdavi, M.A., Morgan, K.H., McCall, G.J.H., Huber, H., 1979. Fannuj Quadrangle Map 1:250000. Ministry of Mines and Metal, Geological Survey of Iran, Tehran.

Esmaeili, R., Xiao, W., Griffin, W.L., Moghadam, H.S., Zhang, Z., Ebrahimi, M., Zhang, J., Wan, B., Ao, S., Bhandari, S., 2020. Reconstructing the source and growth of the Makran Accretionary Complex: Constraints from detrital zircon U-Pb geochronology. Tectonics 39 (2). https://doi.org/10.1029/2019TC005963.

Esmaeili, R., Ao, S., Shafaii Moghadam, H., Zhang, Z., Griffin, W.L., Ebrahimi, M., Xiao, W., Wan, B., Bhandari, S., 2022. Amphibolites from Makran accretionary complex record Permian-Triassic Neo-Tethyan evolution. Int. Geol. Rev. 64 (11), 1594–1610. https://doi.org/10.1080/00206814.2021.1946663.

Festa, A., Dilek, Y., Mittempergher, S., Ogata, K., Pini, G.A., Remitti, F., 2018. Does subduction of mass transport deposits (MTDs) control seismic behavior of shallow–level megathrusts at convergent margins? Gondwana Res. 60, 186–193. https://doi.org/10.1016/j.gr.2018.05.002.

Festa, A., Pini, G.A., Ogata, K., Dilek, Y., 2019. Diagnostic features and field-criteria in recognition of tectonic, sedimentary and diapiric mélanges in orogenic belts and exhumed subduction-accretion complexes. Gondwana Res. 74, 7–30. https://doi.org/10.1016/j.gr.2019.01.003.

Festa, A., Barbero, E., Remitti, F., Ogata, K., Pini, G.A., 2022. Mélanges and chaotic rock units: Implications for exhumed subduction complexes and orogenic belts. Geosyst. Geoenviron. 1 (2), 100030. https://doi.org/10.1016/j.geogeo.2022.100030.

Frassi, C., Di Rosa, M., Farina, F., Pandolfi, L., Marroni, M., 2022. Anatomy of a deformed upper crust fragment from western Alpine Corsica (France): insights into continental subduction processes. Int. Geol. Rev. 1–21. https://doi.org/10.1080/00206814.2022.2031315.

Geersen, J., Ranero, C.R., Barckhausen, U., Reichert, C., 2015. Subducting seamounts control interplate coupling and seismic rupture in the 2014 Iquique earthquake area. Nat. Commun. 6 (1), 8267. https://doi.org/10.1038/ncomms9267.

Glennie, K.W., Hughes Clarke, M.W., Boeuf, M.G.A., Pilaar, W.F.H., Reinhardt, B.M., 1990. Inter-relationship of Makran-Oman Mountains belts of convergence. In: Robertson, A.H.F., Searle, M.P., Ries, A.C. (Eds.), the Geology and Tectonics of the Oman Region. Geological Society, London, Special Publications, pp. 773–786.

Haberland, C., Mokhtari, M., Babaei, H.A., Ryberg, T., Masoodi, M., Partabian, A., Lauterjung, J., 2021. Anatomy of a crustal-scale accretionary complex: Insights from deep seismic sounding of the onshore western Makran subduction zone, Iran. Geology

UNCORRECTED PROOF

49 (1), 3–7. https://doi.org/10.1130/G47700.1.
Hashimoto, Y., Enjoji, M., Sakaguchi, A., Kimura, G., 2002. P-T conditions of cataclastic deformation associated with underplating: An example from the Cretaceous Shimanto complex, Kii Peninsula, SW Japan. Earth, Planets Space 54 (11), 1133–1138. https://doi.org/10.1186/BF03353314.
Hillier, J.K., Watts, A.B., 2007. Global distribution of seamounts from ship-track bathymetry data. Geophys. Res. Lett. 34 (13), L13304. https://doi.org/10.1029/2007GL029874.
Hunziker, D., 2014. Magmatic and metamorphic history of the North Makran ophiolites and blueschists (SE Iran): Influence of Fe^{3+}/Fe^{2+} ratios in blueschist facies minerals on geothermobarometric calculations, ETH Zurich, Switzerland, p. 364. PhD Thesis.
Hunziker, D., Burg, J.-P., Bouilhol, P., von Quadt, A., 2015. Jurassic rifting at the Eurasian Tethys margin: Geochemical and geochronological constraints from granitoids of North Makran, southeastern Iran. Tectonics 34, 571–593. https://doi.org/10.1002/2014TC003768.
Hunziker, D., Burg, J.-P., Moulas, E., Reusser, E., Omrani, J., 2017. Formation and preservation of fresh lawsonite: Geothermobarometry of the North Makran Blueschists, southeast Iran. J. Metamorph. Geol. 35 (8), 871–895. https://doi.org/10.1111/jmg.12259.
Hyndman, R.D., Yamano, M., Oleskevich, D.A., 1997. The seismogenic zone of subduction thrust faults. Isl. Arc 6 (3), 244–260. https://doi.org/10.1111/j.1440-1738.1997.tb00175.x.
Isozaki, Y., 1997. Contrasting two types of orogen in Permo-Triassic Japan: Accretionary versus collisional. Isl. Arc 6, 2–24. https://doi.org/10.1111/j.1440-1738.1997.tb00038.x.
Isozaki, Y., Maruyama, S., Furuoka, F., 1990. Accreted oceanic materials in Japan. Tectonophysics 181, 179–205. https://doi.org/10.1016/0040-1951(90)90016-2.
Kerr, A.C., Tarney, J., Nivia, A., Marriner, G.F., Saunders, A.D., 1998. The internal structure of oceanic plateaus: inferences from obducted Cretaceous terranes in western Colombia and the Caribbean. Tectonophysics 292 (3–4), 173–188. https://doi.org/10.1016/S0040-1951(98)00067-5.
Kimura, G., Ludden, J., 1995. Peeling oceanic crust in subduction zones. Geology 23 (3), 217–220. https://doi.org/10.1130/0091-7613(1995)023<0217:POCISZ>2.3.CO;2.
Kimura, G., Mukai, A., 1991. Underplated units in an accretionary complex: Melange of the Shimanto Belt of eastern Shikoku, southwest Japan. Tectonics 10 (1), 31–50. https://doi.org/10.1029/90TC00799.
Kirkpatrick, J.D., Fagereng, Å., Shelly, D.R., 2021. Geological constraints on the mechanisms of slow earthquakes. Nature Rev. Earth Environ. 2 (4), 285–301. https://doi.org/10.1038/s43017-021-00148-w.
Kodaira, S., Takahashi, N., Nakanishi, A., Miura, S., Kaneda, Y., 2000. Subducted seamount imaged in the rupture zone of the 1946 Nankaido earthquake. Science 289, 104–106. https://doi.org/10.1126/science.289.5476.104.
Kusky, T.M., Bradley, D.C., 1999. Kinematic analysis of mélange fabrics: examples and applications from the McHugh Complex, Kenai Peninsula, Alaska. J. Struct. Geol. 21 (12), 1773–1796. https://doi.org/10.1016/S0191-8141(99)00105-4.
Kusky, T.M., Windley, B.F., Safonova, I., Wakita, K., Wakabayashi, J., Polat, A., Santosh, M., 2013. Recognition of ocean plate stratigraphy in accretionary orogens through Earth history: A record of 3.8 billion years of sea floor spreading, subduction, and accretion. Gondwana Res. 24, 501–547. https://doi.org/10.1016/j.gr.2013.01.004.
Lallemand, S., Culotta, R., Von Huene, R., 1989. Subduction of the Daiichi Kashima seamount in the Japan Trench. Tectonophysics 160, 231–247.
Lallemand, S., Le Pichon, X., 1987. Coulomb wedge model applied to the subduction of seamounts in the Japan Trench. Geology 15 (11), 1065–1069.
Leake, B.E., Wooley, A.R., Arps, C.E.S., Birch, W.D., Gilbert, M.C., Grice, J.D., Hawthorne, F.C., Kato, A., Kisch, H.I., Krivivichev, V.G., Linthout, K., Laird, J., Mandarino, J.A., Maresch, W.V., Nickel, E.H., Rock, N.M.S., Schumacher, J.C., Smith, D.C., Stephenson, N.C.N., Ungaretti, L., Whittaker, E., Youzhi, G., 1997. Nomenclature of Amphiboles. Report of the subcommittee on amphiboles of the International Mineralogical Association Commission on New Minerals and Mineral Names. Mineral. Mag. 61, 259–321.
MacPherson, G.J., 1983. The Snow Mountain Volcanic Complex: An On-Land Seamount in the Franciscan Terrain, California. J. Geol. 91 (1), 73–92. https://doi.org/10.1086/628745.
Manzotti, P., Ballèvre, M., Pitra, P., Schiavi, F., 2021. Missing lawsonite and paragonite found: P-T and fluid composition in meta-marls from the Combin Zone (Western Alps). Contrib. Mineral. Petrol. 176, 60. https://doi.org/10.1007/s00410-021-01818-0.
Marroni, M., Meneghini, F., Pandolfi, L., 2004. From accretion to exhumation in a fossil accretionary wedge: a case history from Gottero unit (Northern Apennines, Italy). Geodin. Acta 17 (1), 41–53. https://doi.org/10.3166/ga.17.41-53.
Maruyama, S., Liou, J.G., 1989. Possible depth limit for underplating by a seamount. Tectonophysics 160 (1–4), 327–337. https://doi.org/10.1016/0040-1951(89)90399-5.
McCall, G.J.H., 1985. Explanatory text of the Minab Quadrangle Map 1: 250 ,000; No. J13. Geological Survey of Iran, Tehran, p. 530.
McCall, G.J.H., Kidd, R.G.W., 1982. The Makran, Southeastern Iran: the anatomy of a convergent plate margin active from Cretaceous to Present. Geol. Soc. Lond. Spec. Publ. 10 (1), 387–397. https://doi.org/10.1144/GSL.SP.1982.010.01.26.
McCall, G.J.H., 2002. A summary of the geology of the Iranian Makran. in: Clift, P.D., Kroon, F.D., Gaedecke, C., Craig, J. (Eds.), The Tectonic and Climatic Evolution of the Arabian Sea Region. Geological Society of London, Special Publications 195, 147-204.
Meneghini, F., Marroni, M., Moore, J.C., Pandolfi, L., Rowe, C.D., 2009. The processes of underthrusting and underplating in the geologic record: structural diversity between the Franciscan Complex (California), the Kodiak Complex (Alaska) and the Internal Ligurian Units (Italy). Geol. J. 44 (2), 126–152.
Meneghini, F., Pandolfi, L., Marroni, M., 2020. Recycling of heterogeneous material in the subduction factory: evidence from the sedimentary mélange of the Internal Ligurian Units, Italy. J. Geol. Soc. 177 (3), 587–599. https://doi.org/10.1144/jgs2019-081.
Moghadam, H.S., Arai, S., Griffin, W.L., Khedr, M.Z., Saccani, E., Henry, H., O'Reilly, S.Y., Ghorbani, G., 2022. Geochemical variability among stratiform chromitites and ultramafic rocks from Western Makran, South Iran. Lithos 412–413, 106591. https://doi.org/10.1016/j.lithos.2021.106591.
Mohammadi, A., Burg, J.-P., Winkler, W., Ruh, J., von Quadt, A., 2016. Detrital zircon and provenance analysis of Late Cretaceous-Miocene onshore Iranian Makran strata: Implications for the tectonic setting. Geol. Soc. Am. Bull. 128 (9–10), 1481–1499. https://doi.org/10.1130/B31361.1.
Mohammadi, A., Burg, J.-P., Guillong, M., von Quadt, A., 2017. Arc magmatism witnessed by detrital zircon U-Pb geochronology, Hf isotopes and provenance analysis of Late Cretaceous-Miocene sandstones of onshore western Makran (SE Iran). Am. J. Sci. 317 (8), 941–964. https://doi.org/10.2475/08.2017.03.
Omrani, H., Moazzen, M., Oberhänsli, R., Moslempour, M.E., 2017. Iranshahr blueschist: subduction of the inner Makran oceanic crust. J. Metamorph. Geol. 35 (4), 373–392. https://doi.org/10.1111/jmg.12236.
Pandolfi, L., Barbero, E., Marroni, M., Delavari, M., Dolati, A., Di Rosa, M., Frassi, C., Langone, A., Farina, F., MacDonald, C., Saccani, E., 2021. The Bajgan Complex revealed as a Cretaceous ophiolite-bearing subduction complex: A key to unravel the geodynamics of Makran (southeast Iran). J. Asian Earth Sci. 222. https://doi.org/10.1016/j.jseaes.2021.104965.
Park, J.-O., Tsuru, T., Kaneda, Y., Kono, Y., Kodaira, S., Takahashi, N., Kinoshita, H., 1999. A subducting seamount beneath the Nankai Accretionary Prism off Shikoku, southwestern Japan. Geophys. Res. Lett. 26 (7), 931–934. https://doi.org/10.1029/1999GL900134.
Platt, J.P., 1986. Dynamics of orogenic wedges and the uplift of high-pressure metamorphic rocks. Geol. Soc. Am. Bull. 97 (9), 1037–1053. https://doi.org/10.1130/0016-7606(1986)97<1037:DOOWAT>2.0.CO;2.
Platt, J.P., 1993. Exhumation of high-pressure rocks: a review of concepts and processes. Terra Nova 5, 119–133.
Platt, J.P., Leggett, J.K., Young, J., Raza, H., Alam, S., 1985. Large-scale sediment underplating in the Makran accretionary prism, southwest Pakistan. Geology 13, 507–511. https://doi.org/10.1130/0091-7613(1985)13<507:LSUITM>2.0.CO;2.
Poli, S., Schmidt, M.W., 2002. The high-pressure stability of hydrous phases in orogenic belts: an experimental approach on eclogite forming processes. Tectonophysics 273, 169–184.
Ramsay, J.G., 1967. Folding and Fracturing of Rocks. Mc Graw and Hill ed., 568 pp.
Ruh, J.B., 2016. Submarine landslides caused by seamounts entering accretionary wedge systems. Terra Nova 28 (3), 163–170. https://doi.org/10.1111/ter.12204.
Ruh, J.B., 2020. Numerical modeling of tectonic underplating in accretionary wedge systems. Geosphere 16 (6), 1385–1407. https://doi.org/10.1130/GES02273.1.
Ruh, J.B., Sallarès, V., Ranero, C.R., Gerya, T., 2016. Crustal deformation dynamics and stress evolution during seamount subduction: High-resolution 3-D numerical modeling. J. Geophys. Res.: Solid Earth 121 (9), 6880–6902. https://doi.org/10.1002/2016JB013250.
Saccani, E., Delavari, M., Dolati, A., Marroni, M., Pandolfi, L., Chiari, M., Barbero, E., 2018. New insights into the geodynamics of Neo-Tethys in the Makran area: Evidence from age and petrology of ophiolites from the Coloured Mélange Complex (SE Iran). Gondwana Res. 62, 306–327. https://doi.org/10.1016/j.gr.2017.07.013.
Saccani, E., Delavari, M., Dolati, A., Pandolfi, L., Barbero, E., Tassinari, R., Marroni, M., 2022a. Geochemistry of basaltic blueschists from the Deyader Metamorphic Complex (Makran Accretionary Prism, SE Iran): New constraints for magma generation in the Makran sector of the Neo-Tethys. J. Asian Earth Sci. 228, 105141. https://doi.org/10.1016/j.jseaes.2022.105141.
Saccani, E., Delavari, M., Dolati, A., Pandolfi, L., Barbero, E., Brombin, V., Marroni, M., 2022b. Geochemistry of volcanic rocks and dykes from the Remeshk-Mokhtarabad and Fannuj-Maskutan Ophiolites (Makran Accretionary Prism, SE Iran): New constraints for magma generation in the Middle East Neo-Tethys. Geosyst. Geoenviron. 100140. https://doi.org/10.1016/j.geogeo.2022.100140.
Safonova, I., Maruyama, S., Kojima, S., Komiya, T., Krivonogov, S., Koshida, K., 2016. Recognizing OIB and MORB in accretionary complexes: A new approach based on ocean plate stratigraphy, petrology and geochemistry. Gondwana Res. 33, 92–114. https://doi.org/10.1016/j.gr.2015.06.013.
Samimi Namin, M., 1982. Geological Map of Taherui 1:250000 Scale. Tehran: Ministry of Mines and Metal, Geological Survey of Iran.
Samimi Namin, M., 1983. Geological Map of Minab 1:250000 Scale. Tehran: Ministry of Mines and Metal, Geological Survey of Iran.
Scholz, C.H., Small, C., 1997. The effect of seamount subduction on seismic coupling. Geology 25 (6), 487–490. https://doi.org/10.1130/0091-7613(1997)025<0487:TEOSSO>2.3.CO;2.
Sun, T., Saffer, D., Ellis, S., 2020. Mechanical and hydrological effects of seamount subduction on megathrust stress and slip. Nat. Geosci. 13 (3), 249–255. https://doi.org/10.1038/s41561-020-0542-0.
Tewksbury-Christle, C.M., Behr, W.M., Helper, M.A., 2021. Tracking deep sediment underplating in a fossil subduction margin: Implications for interface rheology and mass and volatile recycling. Geochem. Geophys. Geosyst. 22 (3). https://doi.org/10.1029/2020GC009463.
Ueda, H., 2005. Accretion and exhumation structures formed by deeply subducted seamounts in the Kamuikotan high-pressure/temperature zone, Hokkaido, Japan. Tectonics 24 (2), TC2007. https://doi.org/10.1029/2004TC001690.
Ukar, E., Cloos, M., 2014. Low-temperature blueschist-facies mafic blocks in the Franciscan mélange, San Simeon, California: Field relations, petrology, and counterclockwise P - T paths. Geol. Soc. Am. Bull. 126 (5–6), 831–856. https://doi.org/10.1130/B30876.1.
Ukar, E., Cloos, M., 2015. Magmatic origin of low-T mafic blueschist and greenstone

CORRECTED PROOF

blocks from the Franciscan mélange, San Simeon, California. Lithos 230, 17–29. https://doi.org/10.1016/j.lithos.2015.05.002.
Vannucchi, P., Fisher, D.M., Bier, S., Gardner, T.W., 2006. From seamount accretion to tectonic erosion: Formation of Osa Mélange and the effects of Cocos Ridge subduction in southern Costa Rica. Tectonics 25 (2), TC2004. https://doi.org/10.1029/2005TC001855.
Vidal, O., Parra, T., 2000. Exhumation paths of high-pressure metapelites obtained from local equilibria for chlorite–phengite assemblage: Geol. J. 35, 139–161.
Vidal, O., De Andrade, V., Lewin, E., Munoz, M., Parra, T., Pascarelli, S., 2006. P-T-deformation-Fe^{2+}/Fe^{3+} mapping at the thin section scale and comparison with XANES mapping: application to a garnet-bearing metapelite from the Sambagawa metamorphic belt (Japan). J. Metamorph. Geol. 24, 669–683.
von Huene, R., Lallemand, S., 1990. Tectonic erosion along the Japan and Peru convergent margins. Geol. Soc. Am. Bull. 102 (6), 704–720.
von Huene, R., Ranero, C., Watts, P., 2004. Tsunamigenic slope failure along the Middle America Trench in two tectonic settings. Mar. Geol. 203 (3–4), 303–317. https://doi.org/10.1016/S0025-3227(03)00312-8.
Wakabayashi, J., 2017. Structural context and variation of ocean plate stratigraphy, Franciscan Complex, California: insight into mélange origins and subduction-accretion processes. Prog. Earth Planet. Sci. 4 (1), 18. https://doi.org/10.1186/s40645-017-0132-y.
Wakita, K., 2015. OPS mélange: a new term for mélanges of convergent margins of the world. Int. Geol. Rev. 57 (5–8), 529–539. https://doi.org/10.1080/00206814.2014.949312.
Wan, B., Wang, X., Liu, X., Cai, K., Xiao, W., Mitchell, R.N., 2021. Long-lived seamount subduction in ancient orogens: Evidence from the Paleozoic South Tianshan. Geology 49 (5), 531–535. https://doi.org/10.1130/G48547.1.
Wang, K., Bilek, S.L., 2011. Do subducting seamounts generate or stop large earthquakes? Geology 39 (9), 819–822. https://doi.org/10.1130/G31856.1.
Wang, C., Ding, W., Schellart, W.P., Li, J., Dong, C., Fang, Y., Hao, T., Tong, Z., 2021. Effects of multi-seamount subduction on accretionary wedge deformation: Insights from analogue modelling. J. Geodyn. 145, 101842. https://doi.org/10.1016/j.jog.2021.101842.
Watts, A., Koppers, A., Robinson, D., 2010. Seamount subduction and earthquakes. Oceanography 23 (1), 166–173. https://doi.org/10.5670/oceanog.2010.68.
Wessel, P., Sandwell, D., Kim, S.-S., 2010. The global seamount census. Oceanography 23 (1), 24–33. https://doi.org/10.5670/oceanog.2010.60.
Yang, G., Li, Y., Xiao, W., Tong, L., 2015. OIB-type rocks within West Junggar ophiolitic mélanges: Evidence for the accretion of seamounts. Earth-Sci. Rev. 150, 477–496. https://doi.org/10.1016/j.earscirev.2015.09.002.
Yang, G., Li, Y., Zhu, Z., Li, H., Tong, L., Zeng, R., 2022. Seamount subduction and accretion in West Junggar, NW China: A review. Geosyst. Geoenviron. 100074. https://doi.org/10.1016/j.geogeo.2022.100074.
Zeng, M., Zhang, R., Chen, S., Liu, X., Li, C., Ettensohn, F.R., Bie, L., 2021. Reconstructing Ocean-Plate Stratigraphy (OPS) to understand accretionary style and mélange fabric: Insights from the Bangong-Nujiang Suture (Tibet, China). Geophys. Res. Lett. 48 (18), 1–12. https://doi.org/10.1029/2021GL094457.

CORRECTED PROOF